2014

The Effect of Surface Corrosion Damage on the Fatigue Life of Extruded Aluminum Alloy 6061-T6

Matthew Weber
University of North Florida, n00853484@ospreys.unf.edu

The Effect of Surface Corrosion Damage on the Fatigue Life of Extruded Aluminum Alloy 6061-T6

by

Matthew Weber

A thesis submitted to the School of Engineering

in partial fulfillment of the requirements for the degree of

Master of Science in Mechanical Engineering

UNIVERSITY OF NORTH FLORIDA

COLLEGE OF COMPUTING, ENGINEERING and CONSTRUCTION

July, 2014

Certificate of Approval

The thesis of Matthew Weber is approved by: Date

_____ _____

Dr. Paul Eason, Ph.D., PE, Advisor

_____ _____

Dr. Murat Tiryakioğlu, Ph.D., CQE, Committee Member

_____ _____

Dr. Juan Aceros, Ph.D., Committee member

Accepted for the School of Engineering

_____ _____

Director of the School of Engineering, Dr. Murat Tiryakioğlu, Ph.D., CQE

Accepted for the College of Computing, Engineering, and Construction

_____ _____

Dr. Mark A. Tumeo, Ph.D., PE,
Dean of the College of Computing, Engineering, and Construction

Accepted for the University

_____ _____

Dr. John Kantner, Ph.D
Dean of The Graduate School

Acknowledgements

The completion of this degree is the culmination of learning a new problem-solving algorithm. Through my engineering education I have learned new ways to approach practical problems and systems of analysis. I have had the pleasure of working with great faculty while at the University of North Florida, many of whom were very instrumental in my success as a graduate student.

I would like to thank my committee for their support and help on this thesis. Special thanks are due to Dr. Paul Eason. He has been essential to my completion of this degree. He brought me into his research group when many others seemed unwilling. His understanding, patience, and desire to see me succeed, are just some of the reasons why I have been successful while here. Without his help, completion of this program would have been more difficult. I would also like to thank Dr. Murat Tiryakioğlu for his help with this thesis. Our conversations regarding the statistical treatment of the data was essential to this thesis. Additionally, without Dr. Tiryakioğlu, getting the samples that I experimented on would not have been possible.

Lastly, I would also like to thank my parents for their continued support. Without them I would not be where I am today.

TABLE OF CONTENTS

LIST OF FIGURES

LIST OF TABLES

LIST OF SYMBOLS AND ABBREVIATIONS

AA – Aluminum Alloy

a - crack length

β – Precipitate of AA 6061-T6 (Mg_2Si)

β '– Precipitate of AA 6061-T6 (Mg_2Si)

β " – Precipitate of AA 6061-T6 (Mg_xSi)

ΔK – Stress intensity

ΔK_{th} – Threshold stress intensity

EPFM – Elastic Plastic Fracture Mechanics

FCC – Face Centered Cubic

GBD – Grain boundary decohesion

GDP – Gross Domestic Product

LEFM – Linear Elastic Fracture Mechanics

MPa – Megapascal

N – Number of Cycles

σ or S = Applied stress

SEM – Scanning Electron Microscope

SSS – Solid State Solution

ABSTRACT

Aluminum alloy 6061-T6 is a common engineering material used in aerospace, automotive, structural applications. Despite its wide use, little has been published about the effects of damage from surface corrosion on its fatigue life. An investigation was performed where 6061-T6 extrusions were exposed to a 3.5% NaCl solution at pH 2 for 2 days and 24 days. The length of time and pH were chosen in order to create distinct surface flaws. The effect of these flaws on the fatigue life was then investigated and analyzed using scanning electron microscopy (SEM) and Weibull statistics. It was determined that samples corroded for both 2-days and 24-days exhibit fatigue lives that can be described using a 3-parameter Weibull distribution. The result of which was the determination of a threshold value for fatigue as well a general understanding of flaw geometry.

Chapter 1: Introduction

Repair and remediation of corrosion in the United States costs roughly $276 billion a year; that is nearly 3% of the nations GDP and that cost is constantly increasing [1]. Additionally, failure due to fatigue accounts for nearly 90% of all mechanical failure [2]. Combined, corrosion and fatigue are a costly design problem for engineers, particularly in the aerospace, automotive, and gas/oil industries. A thorough understanding of both corrosion and fatigue allow engineers to make better decisions with regards to material selection for applications where environmental factors and cyclical loading are unfavorable.

Much of the literature regarding the application of aluminum alloys focuses on corrosion fatigue, and experiments are typically performed using high strength aluminum alloy used in aerospace applications, such as the 2xxx and 7xxx series alloys. Corrosion fatigue should be distinguished from simple mechanical fatigue because of the difference in crack propagation mechanisms. In corrosion fatigue, the part remains immersed in the corrosive environment thus providing the continued presence of a corrosive species in the fatigue crack tip. Faster crack growth occurs because corrosion mechanisms at the crack tip create material removal and embrittlement phenomena not present in simple mechanical fatigue. This results in accelerated fatigue crack propagation. Many industrial applications of aluminum will experience both corrosion and fatigue simultaneously, thus the understanding of corrosion fatigue is of great importance. Little

has been published on the effects of corrosion damage on the simple mechanical fatigue life of aluminum, after removal from the corrosive environment.

While understanding the mechanical behavior of high strength aluminum alloys is important, other industrially used aluminum alloys exist as well, such as the widely used 6xxx series aluminum alloys. Typical uses of the 6xxx series aluminum alloys are found in automotive, aerospace, marine and structural applications [3]. In many instances of these applications, surfaces are subjected to temporary or one time exposures to corrosive environments, which would result in surface damage, thereby affecting fatigue life.

Less literature is available regarding the corrosion and/or fatigue behavior of the 6xxx series aluminum alloys. Additionally, little has been published on the effect of surface corrosion damage on the fatigue life of aluminum alloy 6061-T6. Through the use of Wöhler (S-N) curves, electron microscopy and Weibull statistics, this thesis will present an investigation of the phenomenological effect of surface corrosion damage on the fatigue behavior of aluminum alloy 6061-T6 extrusions.

Chapter 2: Literature review

2.1 Aluminum alloy 6061-T6

When compared to steel, aluminum is lighter and can be used in many of the same applications. Additionally, aluminum (in its solid form) is nontoxic, has good workability and high strength to weight ratio as an alloy. In 1921, Robert Archer and Zay Jeffries created a new aluminum alloy (AA) [4]. They determined that if aluminum (Al), magnesium (Mg) and silicon (Si) were mixed together, an AA with mechanical properties not available in other metal alloys could be produced. It was not until 1935 that applications for medium strength, heat treatable, metal that could also be anodized or welded were being created [5].

Through modification of the AA that Archer and Jeffries had created, came an improved aluminum alloy, AA 6061. With this new AA, building construction, railroad passenger cars, radio telescope structure, airframes, bridge rails, electrical towers, highway signs, mining equipment and trailers could be produced that previously would have been made from other materials [3].

2.1.2 Chemistry and chemical composition of AA 6061-T6

6xxx aluminum alloys contain up to 8 alloying elements with the main components being aluminum, silicon and magnesium (Table 1) [4, 6].

Table 1. Chemical composition of AA 6061[7]

alloy	Si		Fe		Cu		Mn		Mg		Cr		Zn		Ti		Others	
	min	max	min	max	min	max	min	max	min	max	min	max	min	max	min	max	each max	total max
6061	0.40	0.80	--	0.70	0.15	0.40	--	0.15	0.80	1.20	0.04	0.35	--	0.25	--	0.15	0.05	0.15

Due to the number of potential phases formed by the alloying elements, the microstructure of 6xxx series aluminum alloys can be very complex. A variety of standard treatments to this alloy also add complexity by varying the microstructure. The "T6" designation of the aluminum alloy means that the alloy has been solution treated and artificially aged to peak strength, the specifics of which will be presented later. This process imparts a variety of different precipitates within the aluminum. Such precipitates include but are not limited to β, β' and Q-phase (non-strengthing). It has been suggested in the literature that these precipitates, when adjacent to the free surface, can affect the corrosion process occurring on the surface of the aluminum.

This formulation makes use of the limited solubility of Mg and Si in aluminum to from the precipitate Mg_2Si. Additionally, the chromium (Cr) and manganese (Mn) help stabilize the iron intermetallic $(Fe, Mn, Cr)_3SiAl_{12}$, while copper (Cu) is known to create the intermetallic Q-phase [8, 9].

2.1.3 Microstructure and Heat Treatment

Microstructure is a broad term that covers many features within a material. These features include grain and particle sizes, dislocation densities and particle volume fractions [10]. All of these microstructural features can be affected by the heat treatments that are applied to the metal (Table 2).

The "T" in the heat treatment designation indicates that the metal has first been solution heat-treated [7]. Solution heat-treating is the process by which the alloy is heated to a

specified temperature above the solvus, followed by quenching. The alloy's microstructure is homogenized during the heating process. Through quenching, Mg and Si (as well as other elements) remain in solution, in the aluminum matrix. Precipitates are formed in the subsequent aging process. The aging process takes place at specific time and temperature conditions.

Table 2: Aluminum alloy heat treatment designations and corresponding processes [7]

Heat Treatment	Process
T1	Cooled from an elevated-temperature shaping process and naturally aged to a substantially stable condition
T2	Cooled from an elevated-temperature shaping process, cold worked, and naturally aged to a substantially stable condition
T3	Solution heat treated, cold worked, and naturally aged to a substantially stable condition
T4	Solution heat treated and naturally aged to a substantially stable condition
T5	Cooled from an elevated-temperature shaping process and artificially aged
T6	Solution heat treated and artificially aged
T7	Solution heat treated and overaged or stabilized
T8	Solution heat treated, cold worked, and artificially aged
T9	Solution heat treated, artificially aged, and cold worked
T10	Cooled from and elevated-temperature shaping process, cold worked, and artificially aged

A T6 heat treatment that is applied to the AA 6061 produces a very fine microstructure of very small precipitates. An example of the fine microstructure can be seen in the needle like precipitates shown in Figure 1 as identified by Edwards et al [11]. These needle like precipitates are called β" precipitates and are coherent monoclinic Mg-Si clusters [12]; a sequence of possible precipitates and their order of precipitation is shown (Figure 2).

Graphic redacted, paper copy available upon request to home institution

Figure 1. TEM micrograph on the [001] zone axis of AA 6061-T6 [13]

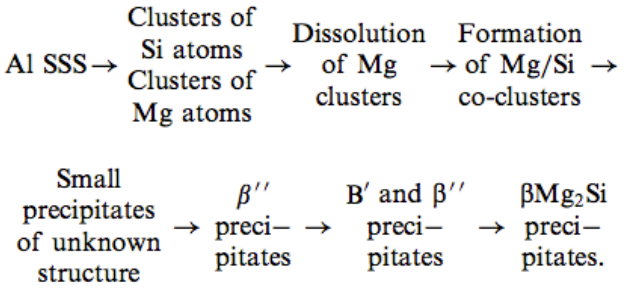

Figure 2. Precipitation sequence in AA 6061. In step 7, B' is also referred to in the literature as Q-phase [11]

2.1.4 Mechanical properties of AA 6061-T6

The chemical composition, the microstructure and heat treatment, as well as its many mechanical and microstructural properties make AA 6061-T6 a primary engineering material. Aluminum has an FCC crystal structure with 12 different slip systems. These slip systems occur along the close packed plane, specifically in the plane of type {111} and in the <110>-type direction. This provides great ductility and toughness. With a tensile strength of 310 MPa, a yield strength of 276 MPa, fatigue strength of 97 MPa at 5 x 10^8 fully reversed cycles and an elongation of 17% [7], AA 6061-T6 is an alloy of choice for many engineering applications.

2.2 Fatigue

Since the 1800's it has been recognized that a metal subjected to repetitive or fluctuating stress will fail at a stress much lower than that required to cause failure upon application of a single load [2]. There typically is not any visible indication that a part is being fatigued, making it difficult to detect and predict eminent failure. Because of this, nondestructive tests, i.e. dye penetrant test, exist to examine structures for flaws and cracks. However, these tests vary in their sensitive and can be costly in large applications [14]. Therefore, understanding how and why materials fatigue, the mechanisms of fatigue crack initiation and propagation, and the predictability of fatigue, is paramount in being able to establish an expected life at a given stress. Once understood, designers can use fatigue life data as a design parameter, like strength or hardness.

2.2.1 The S-N Curve

A common method for graphically representing fatigue data is through the Wöhler stress-life curve, also known as the S-N curve (Figure 3). The S-N curve is a plot of stress (S) against the number of cycles to failure (N).

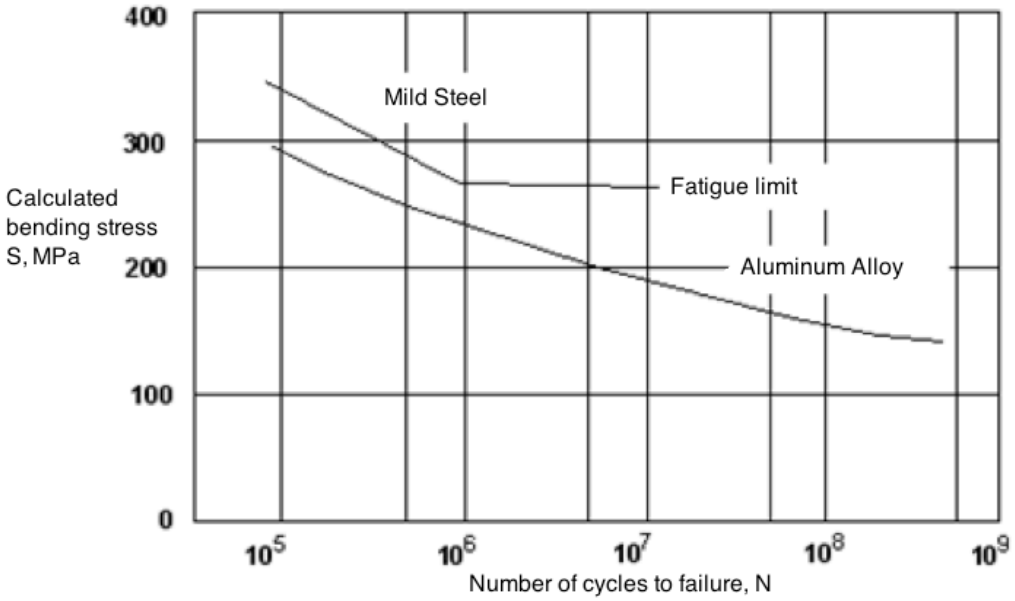

Figure 3. Typical S-N curve for general aluminum and steel alloy. Recreated from [2]

Typically, the nominal applied stress is plotted. This means that the stress is plotted without any consideration of local stress concentrations. In the laboratory, S-N curve data is obtained using axial tension or rotational bending fatigue testers. An axial tension instrument works by applying and releasing a tension load on a test sample as well as recording the number of cycles to failure. A rotational bending instrument works by applying a load to a rotating specimen. Thereby applying tension and compression cyclically to a single point until failure occurs (Figure 4).

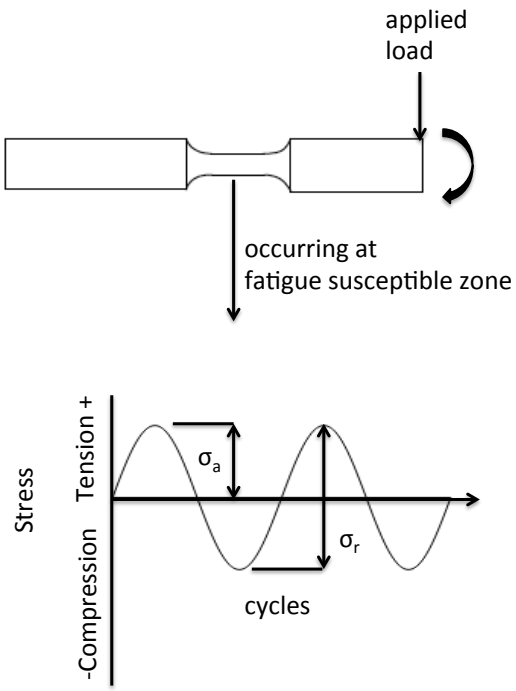

Figure 4. Rotational bending fatigue sample geometry (above) with fully reversed applied load. σ_a is the alternating stress and σ_r is the stress range (below)

Fatigue data are collected from multiple stress states with the first specimen(s) being tested at a high stress, e.g. at about ninety percent of the yield strength, ensuring failure will occur in a fairly short number of cycles. The test stress is successively decreased until one or two specimens do not fail in the specific number of cycles, approximately 10^7 cycles [2]. Although 8-12 specimens can be used to generate a S-N curve, the use of more specimens at each stress level will serve to reduce the error in the curve [2]. Once the data is collected, it is fit using the Basquin equation (eq. 2.1) [15].

$$N\sigma_a^k = C \tag{2.1}$$

N = number of cycles

σ_a = S = the stress amplitude

C = empirical constant

k = Basquin exponent

The application of the Basquin equation to fatigue data allows for the creation of the S-N curve (Figure 5). The Basquin exponent has been shown to be strongly affected by the material as well as the test specimens' geometry [16, 17]. Figure 5 shows the S-N curve for forged and ablation-cast 6061-T6. Tiryakioğlu et al, [18] concluded that the Basquin exponent k for forged and ablation-cast aluminum were within 15% of one another. Thus indicating a similarity between the two materials. This is significant because inclusions or flaws may be present depending on the casting method used.

Graphic redacted, paper copy available upon request to home institution

Figure 5. Wöhler (S-N) curves for ablation-cast and forged 6061-T6 [18]

2.2.2 Regions of Fatigue Life

Fatigue has been shown to take place in three distinct regions. Region I is defined by fatigue crack initiation and is governed by the crack threshold stress intensity factor, ΔK_{th}. Region II is defined by fatigue crack propagation and is governed by the Paris-Erdogan rate law. Region III is defined by fatigue crack fracture and is governed by the crack stress intensity factor, ΔK_c. Figure 6 is a shows a log-log schematic of fatigue crack growth per cycle (da/dN) with respect to the stress concentration factor ΔK. Each region is described in greater detail in the follow sections.

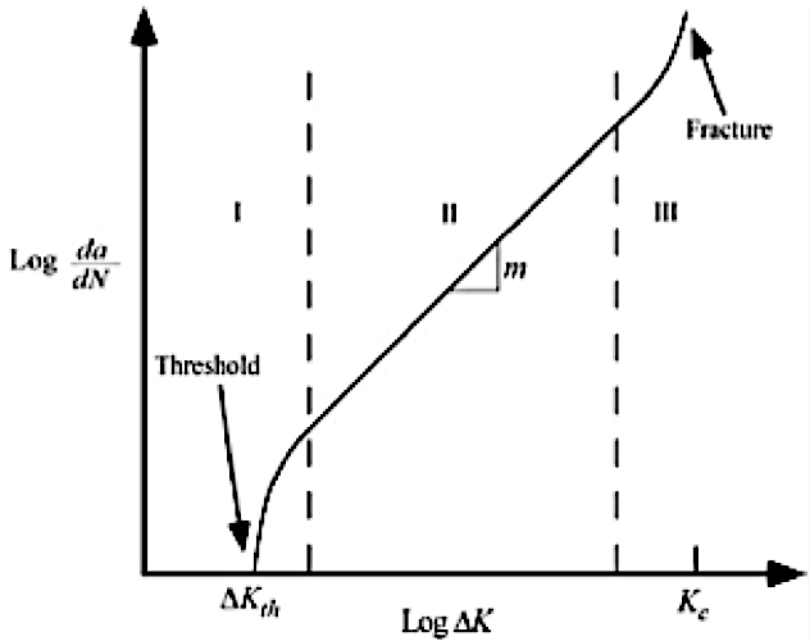

Figure 6. Log-Log plot of fatigue crack initiation behavior in metals. Recreated from [19]

2.2.2.1 Fatigue Crack Initiation: Region I

Often, fatigue failures start at the surface of a material [2, 19-22]. This is because the stress (due to torsion or bending) is at a maximum along the surface. In the case of fatigue, intergranular cracks, inclusions, or surface defects are sources of flaws. If a

surface flaw is present in an area of maximum stress, the result will be a reduction in fatigue life.

In order for a fatigue crack to initiate, a "threshold" criteria that is dependent upon microstructure needs to be met. This threshold can be defined as the mechanism for a critical fatigue flaw to be formed out of microstructural features like, planes, grain boundaries or cleavage facets. Upon satisfaction of the "threshold" criteria, a crack may begin to initiate and grow with each cycle. In the fatigue crack lifecycle, the initiation region is referred to as region I (Figure 7). The fracture surface that is observed as a result of region I often has a flat, faceted appearance, resembling that of cleavage [19]; one such mechanism is grain boundary cracking. Grain boundary cracking is the result of embrittlement at the grain boundary due to dislocation pile-up. The grain boundary crack will continue to propagate along the boundary until it reaches a barrier such as a perpendicularly oriented grain boundary [23-27]. The exposed grain surface can serve as a fatigue initiation flaw.

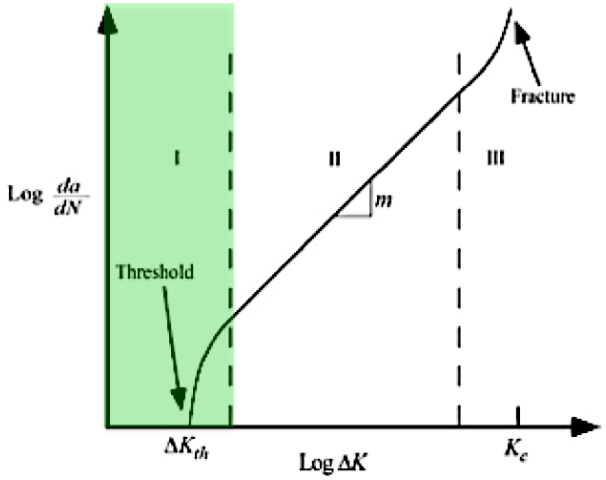

Figure 7. Log-Log plot of fatigue crack initiation behavior in metals with region I being shaded in green. Recreated from [19]

As the crack continues to grow, so will the stress that it imparts to the system. If the stress in a material due to a flaw is to be numerically described, then a combination of Linear Elastic Fracture Mechanics (LEFM) and Elastic Plastic Fracture Mechanics (EPFM) may be used. Much of LEFM is concerned with brittle materials, while EPFM is concerned with materials where ductile deformation dictates fracture behavior. Fracture mechanics is applicable provided a crack can initiate and grow from a flaw of depth a. LEFM is generally regarded as the preferred method for describing fatigue crack initiation mechanisms [28]. Irwin [29] and Orowan [30] determined that the stress at failure for materials that do not explicitly behave as a brittle material, and are capable of plastic flow can be described by:

$$\sigma_f = \sqrt{\frac{2E(\gamma_s + \gamma_p)}{\pi a}} \tag{2.2}$$

σ_f = failure stress

E = Young's modulus

γ_s = total energy of broken bonds in unit area

γ_p = plastic work per unit area of surface created ($\gamma_p > \gamma_s$)

a = crack length

However, equation 2.2 is typically used for single load and single flaw applications. In order to describe the effect of a load on the stress state at the crack tip requires the stress intensity factor, K. The stress intensity factor is defined as:

$$K = \beta\sigma\sqrt{\pi a} \tag{2.3}$$

σ = applied stress

a = crack length

β = geometry factor of flaw

If the applied stress and geometry of the flaw are held constant, then the effect of the stress will be greatest at the crack tip and will dissipate as distance increases away from the flaw (Figure 8). If the applied stress is not constant, then K is represented as ΔK due to the change in stress.

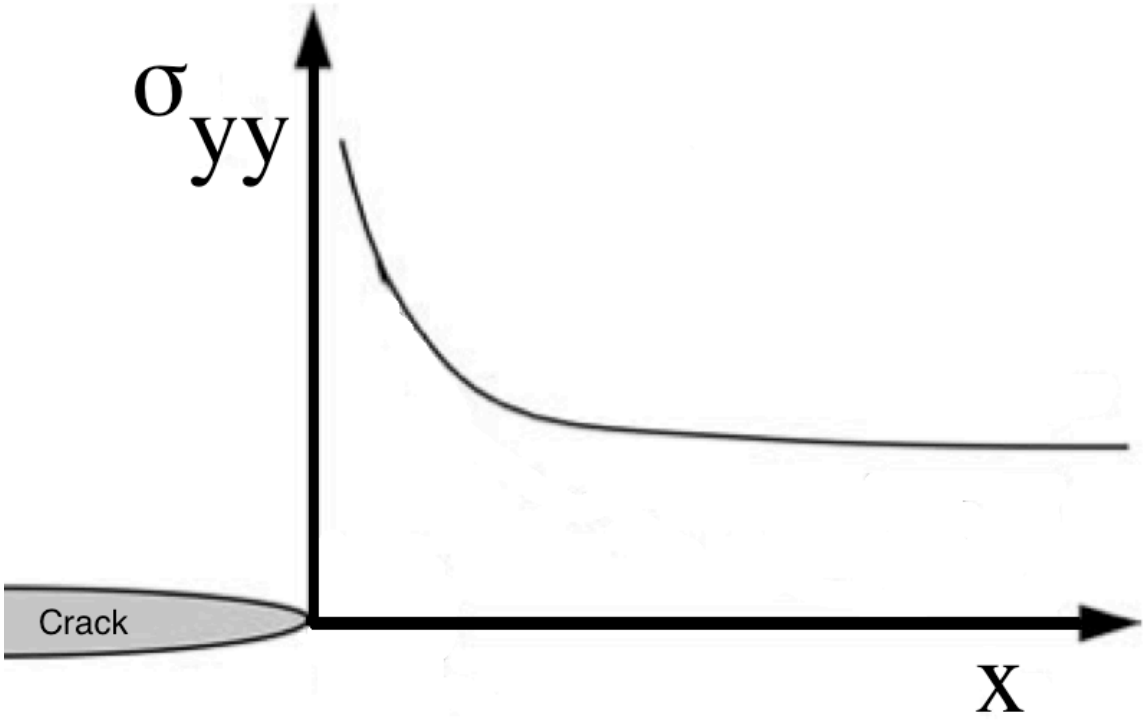

Figure 8. Schematic representation of stresses near the crack tip in an elastic material, per the LEFM model [19]

2.2.2.2 Fatigue Crack Propagation: Region II

In the 1960s Paris and Erdogan [31, 32] demonstrated that fatigue crack growth (Figure 9) is governed by a power law relationship that later became known as the Paris- Erdogan law:

$$\frac{da}{dN} = C\Delta K_{eff}^{m} \tag{2.4}$$

$\frac{da}{dN}$ = the crack growth per cycle

C and m = material constants

$\Delta K_{eff} = K_{max} - K_{min}$ (stress intensity range or crack tip driving force)

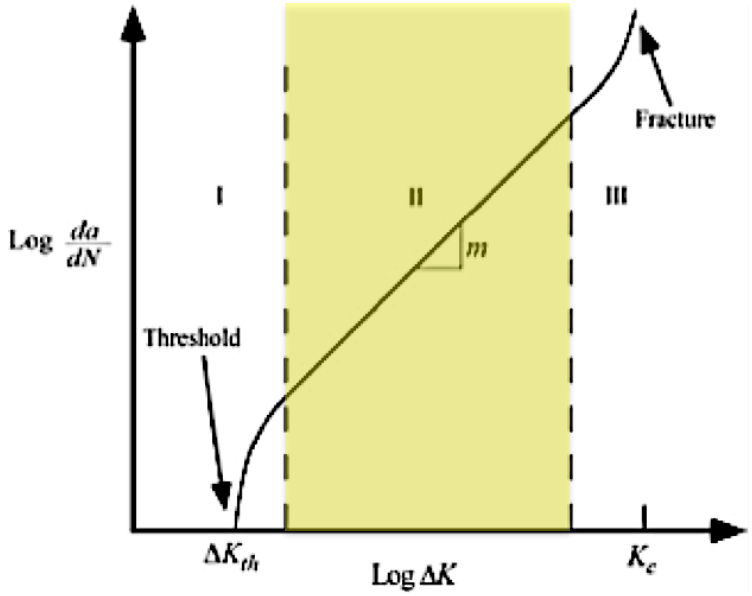

Figure 9. Log-Log plot of fatigue crack propagation behavior in metals with region II shaded in yellow. Recreated from [19]

It was suggested by Paris and Erdogan that the exponent *m* would have a value of 4 [32]. However, subsequent studies have shown that *m* is between 2 and 4 [19] and It has been shown by Weertman [26, 27] that the exponent *m,* is strongly affected by mechanisms including shear sliding and dislocation shielding.

If fatigue crack initiation and propagation (region I and II) are to be described within one equation, then the Klesnil and Lukas modified crack growth law is used [33]:

$$\frac{da}{dN} = C(\Delta K^m - \Delta K_{th}^m) \tag{2.5}$$

This modified law takes into account a crack threshold driving force (ΔK_{th}) in order to describe the first two regions of the curve. If ΔK_{th} equals zero, then description of the fatigue crack curve will take place via the Paris-Erdogan Law. Moreover, much research had been conducted to try and describe the entire curve however; all formulas are derivations of the Paris-Erdogan Law [21, 27, 33-37]. Unlike region I, region II is not microstructurally dependent. Two aluminum alloys with different mechanical properties have been shown to exhibit similar fatigue crack growth characteristics. [36, 38].

The visual evidence of crack growth in a material is often indicated by the formation of striations. Striations are seen as small ridges perpendicular to the direction of crack growth. These striations propagate through the material as the crack continues to grow (Figure 10).

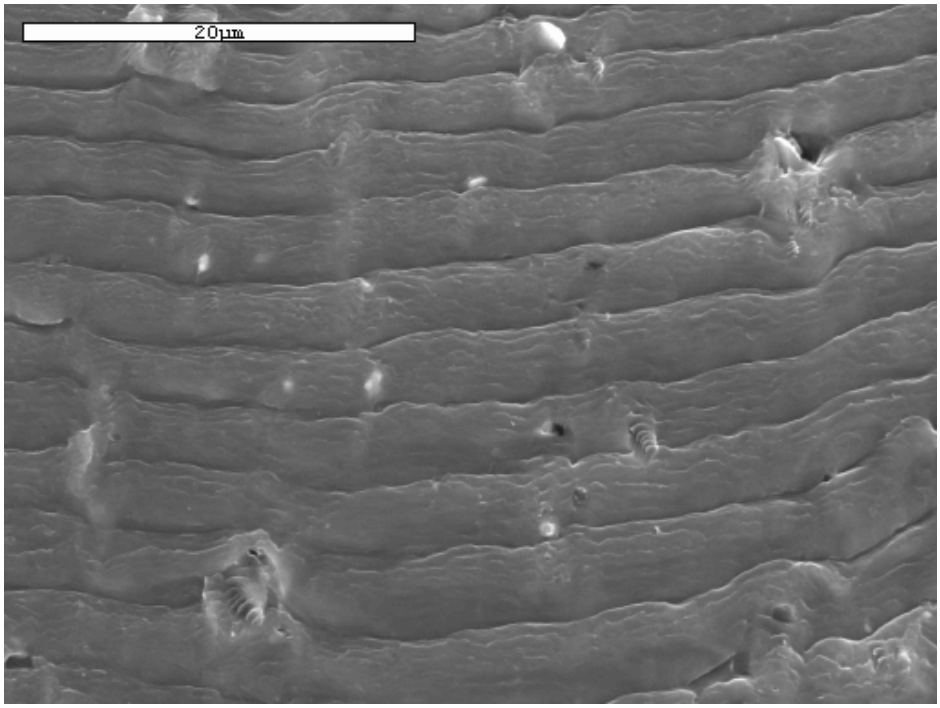

Figure 10. Striations obtained experimentally from fatigue in Aluminum Alloy 6061-T6

It is important to note that fatigue striation creation remains the subject of much debate. Lankford and Davidson [39] observed that depending on the ΔK value, several applications of cyclic load may be required to produce a fatigue striation.

Figure 11 shows one of the proposed mechanisms of fatigue striation creation as reported by Laird [40]. The first step (a to b) is achieved as the load is increased. The crack tips blunts (b to c) and incremental growth occurs. Local slip is constrained to $\pm 45^{o}$ from the crack plane and reverses direction as the load is decreased. The decrease in load causes the crack to fold in on itself (c to d). The process repeats itself as the cyclic load is continually applied (e).

Figure 11. Illustration of the states of crack blunting mechanism for striation formation during fatigue crack growth [40]

2.2.2.3 Fatigue Fracture: Region III

Region III of the crack growth curve is characterized by an increase in the rate of crack growth per cycle partly because as the crack grows larger, the stress concentration at the crack tip becomes large (Figure 12). This region is characterized by the stress concentration ΔK_c, which is the fracture toughness of a material. This value is the related to the amount of stress necessary for final fracture to occur. There is not a large amount of research available regarding region III. This is because, once a fatigue crack has reached a critical size, it is of less relevance due to eminent fracture.

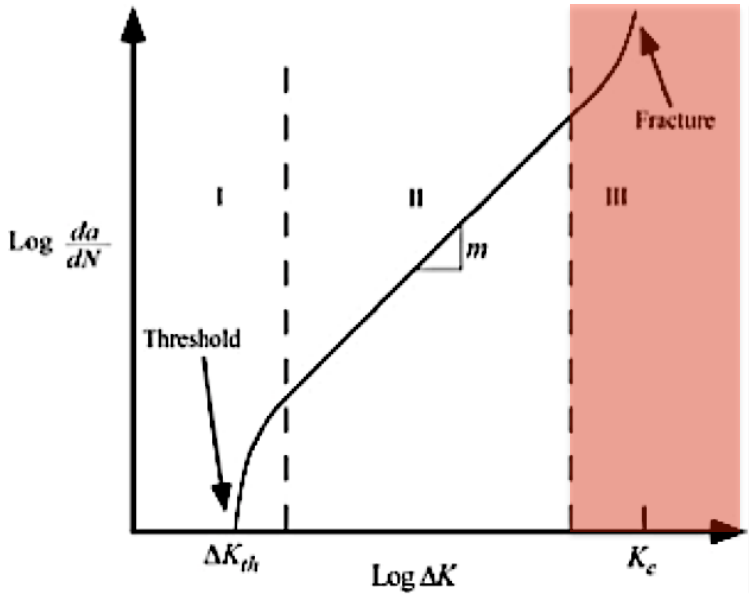

Figure 12. Log-Log plot of fatigue fracture behavior in metals with region III shaded in red. Recreated from [19]

2.2.3 Fatigue and Statistical Analysis

In the mid part of the 20th century, Wallodi Weibull [41-43] came up with an empirical probability distribution that could be used in failure analysis. Weibull, using the "weakest link" theory developed by Pierce [44], was able to show that:

$$P = 1 - exp\left[-\left(\frac{x-x_t}{x_0}\right)^m\right] \tag{2.6}$$

P = the probability of failure at a given stress (strain, fatigue life, etc.) or lower

x = the given perimeter of interest (strain, fatigue life, etc.)

x_t = threshold value below which no failure is expected

x_0 = scale parameter

m = shape parameter (Weibull modulus)

The “weakest link” theory is significant because it makes the assumption that failure will occur at the location where the conditions are the most damaging, i.e. a surface defect, inclusion, etc. that lead to highest local stress

Weibull demonstrated that this probability distribution is effective in predicting material failure due to the aforementioned damaging conditions [18, 41-43, 45, 46]. When the Weibull distribution is linearized to the following equation;

$$Ln(-\ln(1-P)) = m\ln(x - x_t) - m\ln(x_0), \tag{2.7}$$

and plotted, the shape parameter (Weibull modulus) becomes the slope. The curve of best fit can be obtained using the maximum likelihood method. The probability of each point (P) can be assigned using the plotting position formula suggested by Tiryakioğlu et al. [18]:

$$P = \frac{i-0.5}{n} \tag{2.8}$$

i = the rank in ascending order

n = sample size

For a three-parameter Weibull distribution, the presence of a threshold value indicates a point where there is no probability of failure below that stress [18]. Any point beyond the threshold value immediately has a probability of failure. As the measured stress advances past the threshold stress value, the cumulative probability of failure at a given stress becomes greater [41, 42].

Figure 13 shows both two and three-parameter Weibull distributions. For the positive threshold three-parameter distribution, the slope is initially steep (high probability) and

eventually levels out (lower probability). For the two-parameter distribution (no threshold value) the slope is constant indicating that failure is equally probable along the curve. The negative threshold three-parameter distribution indicates that other defects are occurring, requiring further statistical treatment.

Figure 13. The probability plot for three Weibull distributions showing the effect of the threshold value [45]

The Weibull data can also be used to infer flaw geometry distributions [45]. Recall that one of the variables that govern crack propagation is the stress intensity factor, K. In order for the probability of failure to be zero below a certain stress, K needs to be sufficiently small. In order for K to be small, the flaw geometry (β) must be less severe. Therefore, if the threshold value were zero, then flaw geometry would be severe enough to cause failure at any stress. As the threshold value increases, the severity of the flaw geometry decreases (Figure 14).

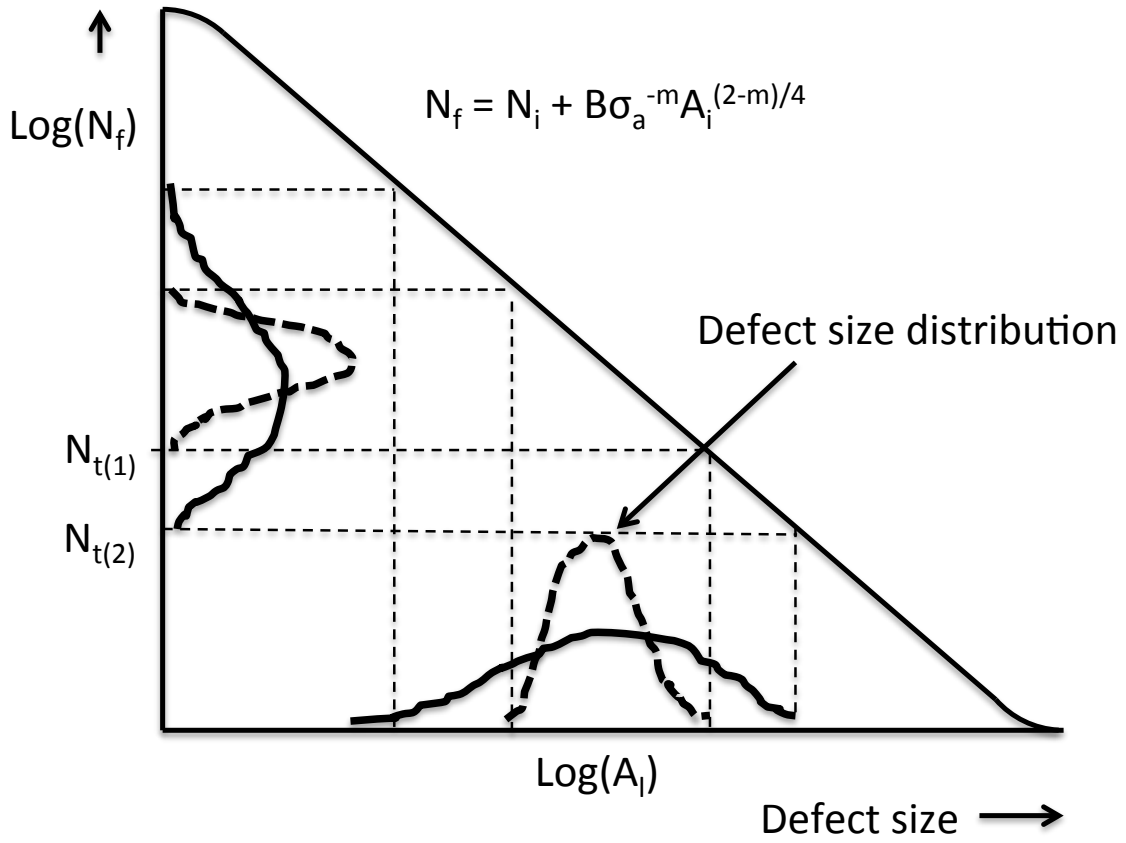

Figure 14. Schematic illustration of the effect of two different defect size distributions on the number of fatigue lives to fracture ($Log(N_f)$) with threshold stress values $Log((N_t))$. The equation of the line is a rearranged Paris-Erdogan equation [47]

2.3 Corrosion

Corrosion has many forms including uniform, galvanic, crevice and pitting, with each of these forms occurring in aqueous conditions. Corrosion often occurs in aqueous environments because water server as the carrier for ions [48]. While the chemistry of corrosion can be quite complex, understanding the process of corrosion allows for engineers to make better-informed decisions when designing for corrosive environments.

2.3.1 Aqueous Chloride Corrosion of Aluminum

A pure sample of solid aluminum will readily oxidize on its surface and form a passive aluminum oxide (Al_2O_3) layer. This passive layer serves to protect the remaining aluminum from most environmental hazards. However, the passive layer is not impervious to the chloride ion, which is a potent corroding species to aluminum [49-51].

Boag et al. [51] stated that pitting caused by chloride attack is one of the most serious forms of corrosion for aluminum alloys. This type of corrosion has been shown to lead to other types of corrosion, as well as structural degradation of aluminum members. Much research has gone into understanding the exact mechanism of corrosion pitting in aluminum [49-54]. It has been shown in very high purity aluminum that the pitting mechanism is controlled by 1) penetration of the oxide layer by chloride ions, 2) thinning of the oxide layer by chloride ions or 3) through easy diffusion paths [51].

Another contributor to chloride ion attack in aluminum alloys is due to intermetallic particles (such as Al_2Cu and $FeAl_3$). It has been shown that corrosion preferentially starts at these particles located along the surface and at grain boundaries [51, 55-71].

Figure 15 shows a schematic of general surface corrosion in aluminum. In Figure 15a aluminum is slowly removed from the passive layer by water. A metal salt island is formed through interaction of the chloride ion with the passive layer (Figure 15b). The increased water solubility of the metal salt island provides greater access for chloride ion attack on the aluminum matrix leading to pitting (local) corrosion (Figure 15c). As

corrosion continues, general surface (global) corrosion will occur leading to uniform surface removal and relatively shallower pits.

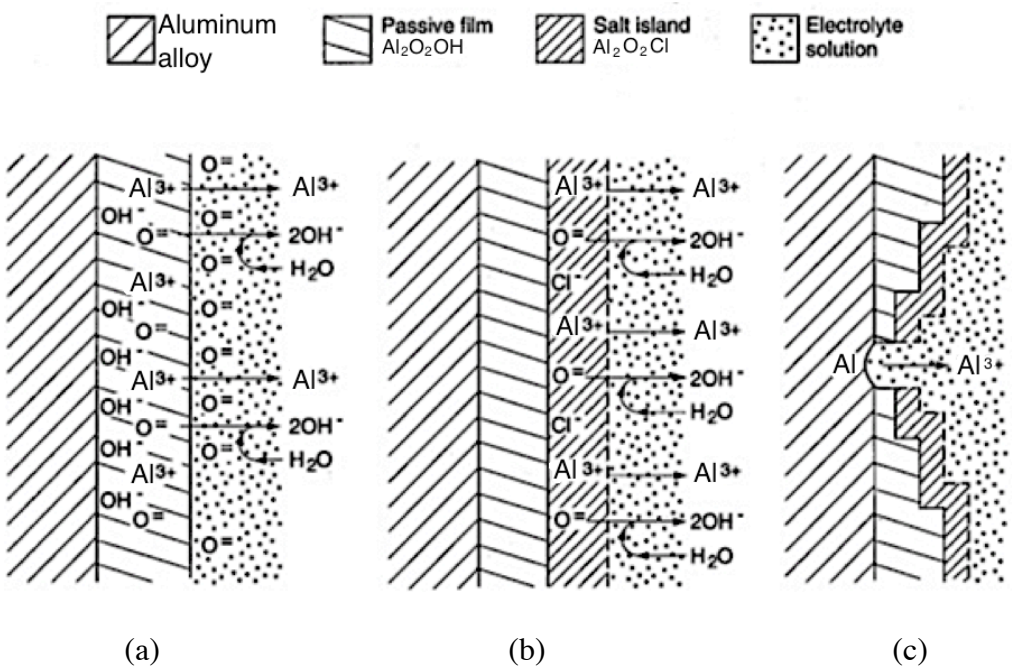

Figure 15. Proposed mechanism occurring during corrosion in aluminum, modified from [48] a) slow dissociation of aluminum ions into solution b) formation of salt island on passive layer c) pit formation and corrosion

There are several published studies on the corrosion behavior of wrought AA 6061-T6 for particular corrosion scenarios [50, 70, 72]. There are number of independent variables that affect the corrosion behavior, including, but not limited to the disposition of phases in the microstructure and the composition of the precipitates, which have all been shown to affect the corrosion kinetics and morphology of AA 6061-T6 [57, 70, 72, 73]. Because of the number of phases, constituents and their possible combinations in the various heat treatments, as well as the complicated nature of their cooperative effects, there is little published on the general nature of corrosion of AA 6061 in any of its numerous heat treatment conditions.

2.3.2 Environmental Effects on Corrosion Pitting

It has been reported that corrosion pit depth increases with time (in the absence of general corrosion) according to a power law and that longer exposure to a corrosive environment will ensure deeper pits [49, 74, 75]:

$$d = Kt^b \tag{2.9}$$

d = pit depth

K and b = empirical constants

t = time

K and b are results of many factors such as charge transfer, mass transport or ohmic effects, and inevitably change with environment and alloy of interest [53, 67]. In a series of papers by Harlow and Wei, a probabilistic approach was taken to determine or predict the rate of pit growth, thereby determining K and b for 2xxx and 7xxx series AA's [57, 59, 67, 76]. They provided a series of conditional cumulative distribution functions that showed the probability of pit size formation given the number of intermetallic particles per particle cluster. They concluded that pitting (at constant temperature, pH and for a specific length of time) generally occurs around clusters of intermetallic particles and that the number of particles per cluster had a direct effect on the rate of pitting.

In 2010, Cavanaugh, performed an applied neural network analysis (ANN) to determine the effect of the aqueous environment on the values of K and b at a variety of different temperatures and pH for 7xxx series AA [77]. In both cases, it was shown that pH and temperature have a significant impact on the rates of corrosion while chloride ion concentration has less of an effect. Cavanaugh [77] was able to create contour maps

representing the rates of corrosion pitting based on temperature and pH (Figure 16 and Figure 17). Cavanaugh established that the time exponent *b* and the constant *K* were environmentally dependent. The largest difference in pitting behavior was observed when cold, acidic conditions were compared to hot, alkaline conditions. It was also observed that in alkaline conditions the time exponent was very small compared to acidic conditions. This is because at an alkaline pH, general corrosion dominates, leading to shallower pits with wider diameters (Figure 18).

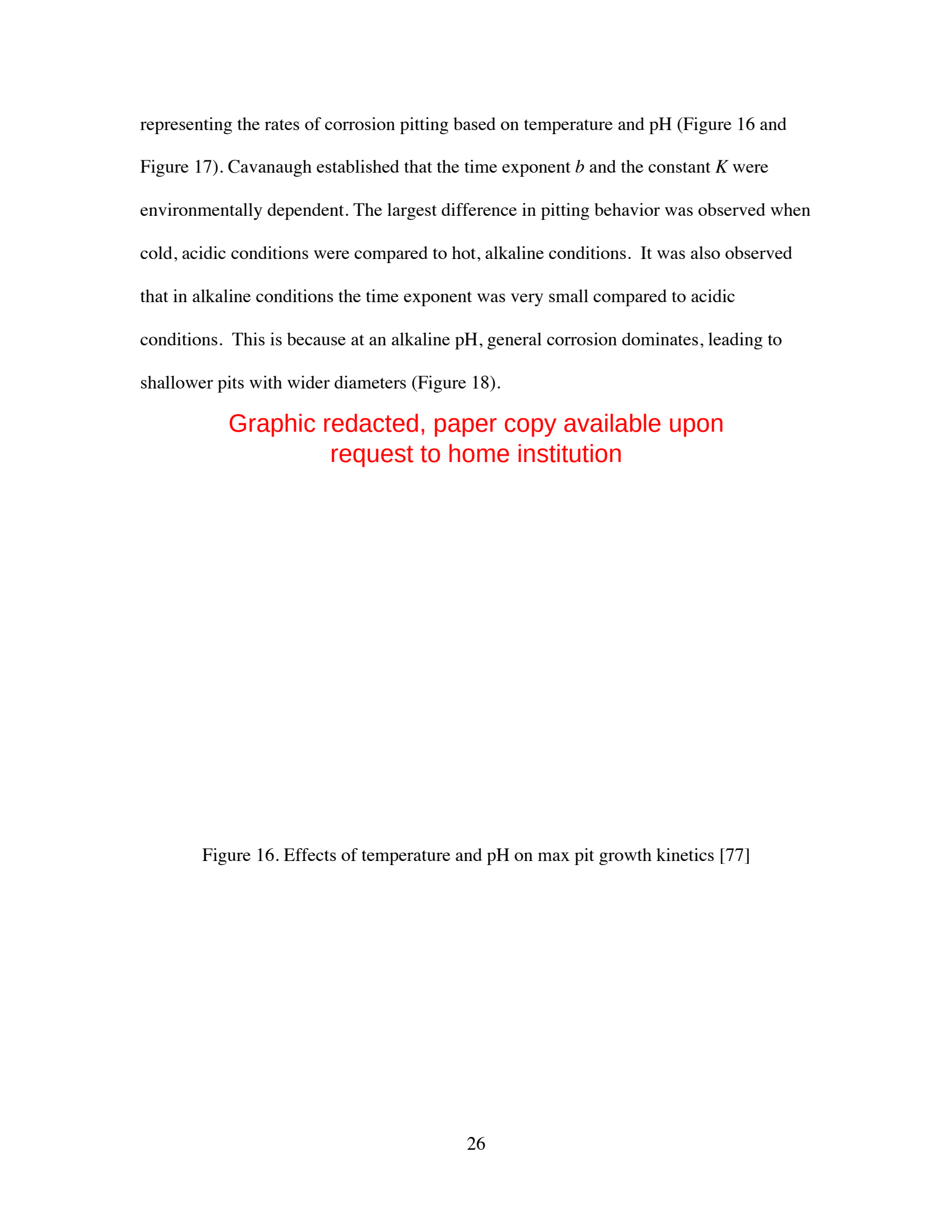

Figure 16. Effects of temperature and pH on max pit growth kinetics [77]

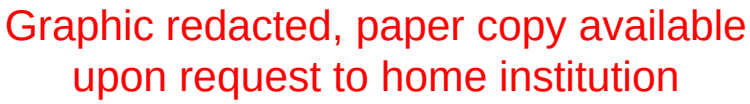

Figure 17. Effects of temperature and pH on median pit growth kinetics [77]

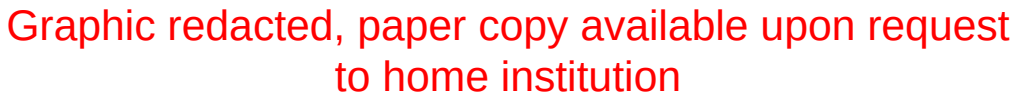

Figure 18: Demonstration of how uniform corrosion will affect the measured pit depth and diameter versus the values in the absence of any uniform corrosion [77]

2.3.3 Corrosion Pit Geometry

Determination of corrosion pit depth and diameter is possible through techniques such as laser profilometry. However, determining the different shapes of the pits beneath the surface is difficult. One of the best method for this analysis is the creation of epoxy replicas of the pits demonstrated by Liao [78]. Figure 19 shows the different kind of pits that may form because of corrosion.

It remains to be determined what causes different pit geometries to form beneath the surface. As suggested in the literature, many different factors affect corrosion pit initiation, growth and morphology [49-53, 56-59, 66, 67, 77-80]. Some factors include but are not limited to constituent particle size and distribution, applied heat treatment of the aluminum, pH and temperature of environment.

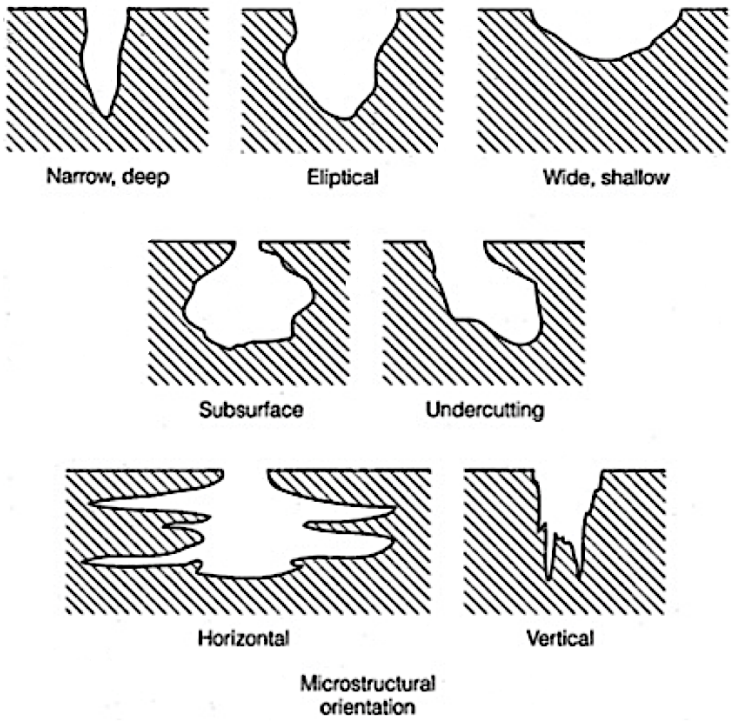

Figure 19. Variations of cross sectional shape of pits formed during corrosion. Recreated from [81]

As previously discussed, stress risers such as a surface corrosion flaw will increase the local stress by a factor of K, the stress intensity factor, thus providing a potential site for fatigue or fracture initiation. If the surface corrosion flaws have varying structure (Figure 19), then K will vary as the flaws do, leading to varied mechanisms for fatigue initiation.

Chapter 3: Experimentation

The purpose of these experiments was to determine the effect of surface corrosion flaws on the fatigue life of AA 6061-T6. Two distinct surface conditions were imposed by exposure of the samples to room temperature, acidic, chloride corrosion and two different time intervals. The purpose of the room temperature and acid conditions was to ensure discrete pit formation, as described from the literature review. Following corrosion, the samples were cleaned and subjected to fatigue tests. The number of cycles to failure was recorded. Following fatigue, certain samples were analyzed by fractographic methods. The fatigue life data were then analyzed to determine the probability of fatigue failure as well as a defect size distribution through Weibull analysis.

3.1 Sample Preparation

Fatigue and tensile specimens were prepared from extusions by Tifton aluminum; Figure 20 and Figure 21 respectively (following page). The AA 6061-T6 samples had a chemical composition provided by Tifton shown in Table 2.

Table 2. Chemical composition of AA 6061 provided by Tifton

alloy	Si		Fe		Cu		Mn		Mg		Cr		Zn		Ti		Others	
	min	max	min	max	min	max	min	max	min	max	min	max	min	max	min	max	each max	total max
6061	0.40	0.80	--	0.70	0.15	0.40	--	0.15	0.80	1.20	0.04	0.35	--	0.25	--	0.15	0.05	0.15

The samples were received as specified to be “polished”; however, significant machine grooves existed (Figure 22). It was observed that the machining grooves were on the same order of magnitude as the proposed corrosion defects. In order to eliminate machine

grooves that would interfere with the study, the samples were polished with 200, 400, 800, and 1200 grit silicon carbide (SiC) paper. Followed by, 1 μm, 0.3 μm, 0.05 μm alumina (Al_2O_3) suspensions. The final step of polishing required 0.04 μm colloidal silica to achieve the final surface. Once polishing was completed, the samples were cleaned using methanol in an ultrasonic bath. Cleaned samples were examined in a Scanning Electron Microscope (SEM) to obtain an "as-reviewed" image before corrosion (Figure 23).

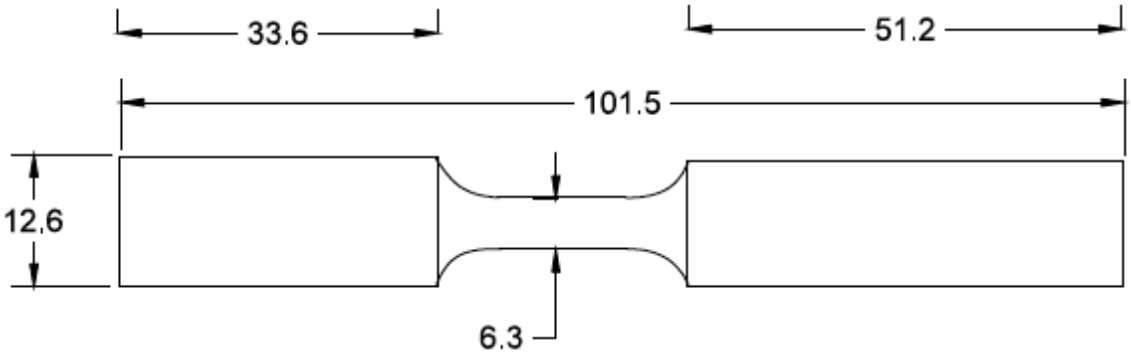

Figure 20. Fatigue specimen geometry. All dimensions are in mm

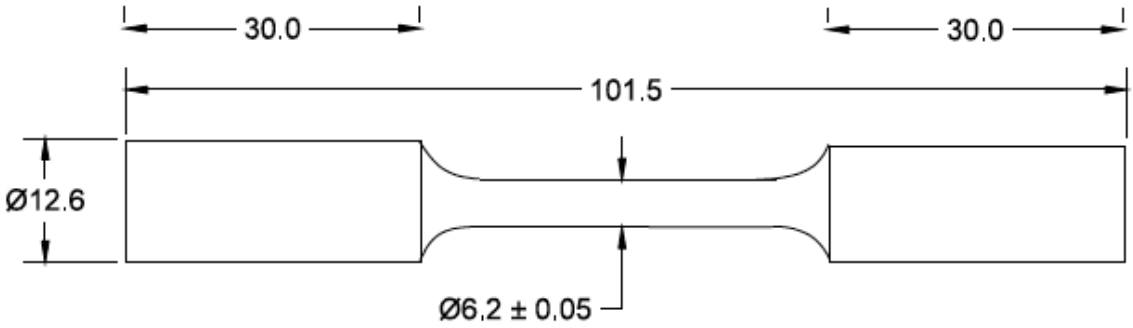

Figure 21. Tensile specimen geometry. All dimensions are in mm

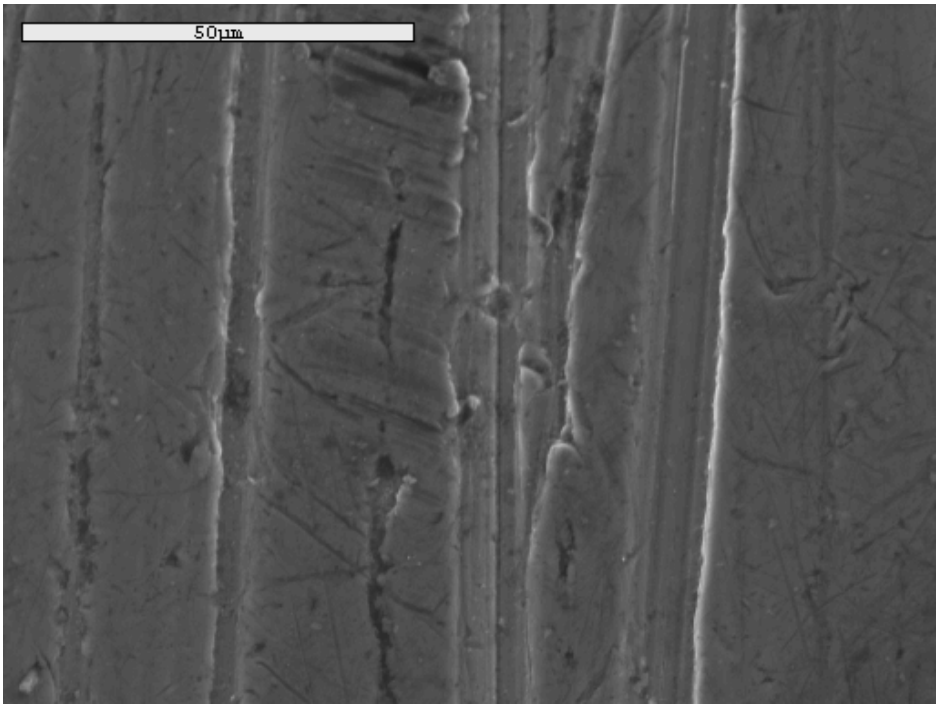

Figure 22. SEM micrograph of unpolished AA 6061-T6 fatigue specimen surface. Note: Machine marks are observed as the vertical features in the image

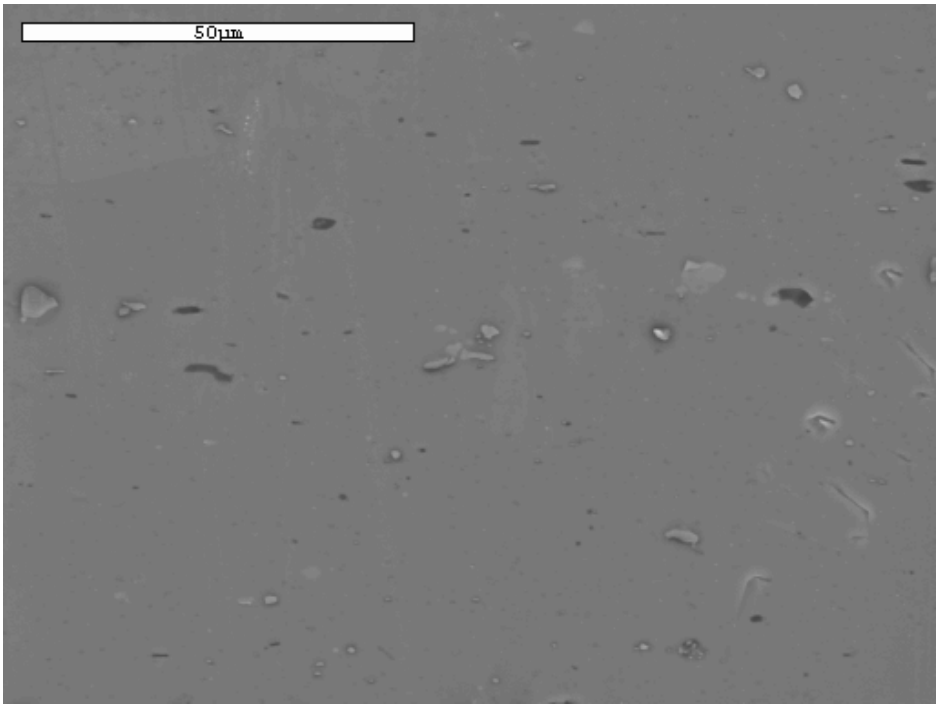

Figure 23. SEM micrograph of polished AA 6061-T6 fatigue specimen surface, indicating removal of machine marks

Before samples could be subjected to fatigue testing, the yield strength of the AA 6061-T6 extrusion had to be determined. In addition, stress values were chosen relative to the yield strength. Three tensile specimens were used to determine the yield strength. Tensile tests were conducted on an Instron 3369 and accompanying extensometer (Figure 24, Table 3). An average yield strength of 255 MPa was measured and used for fatigue analysis. The nominal stress levels used in fatigue testing and the number of AA 6061-T6 extrusions used at each stress level are shown in Table 4.

Table 3: The experimentally determined yield strength and ultimate tensile strength for extruded AA 6061-T6.

	Yield Strength (MPa)	Ultimate Tensile Strength
Tensile Specimen 1	257.3	278.2
Tensile Specimen 2	256.1	273.5
Tensile Specimen 3	253.6	273.8
Average	255.7	275.2

Table 4. The nominal stress levels to be used in fatigue testing and the numbers of AA 6061-T6 specimens tested at each level. Based on experimentally determined yield strength of 255 MPa

σ_{max} (MPa)	230	191	153	128	115	102
σ_{max}/σ_y	0.90	0.75	0.60	0.50	0.45	0.40
number of samples for 2 days	5	5	5	5	4	1
number of samples for 24 days	5	5	5	5	4	1

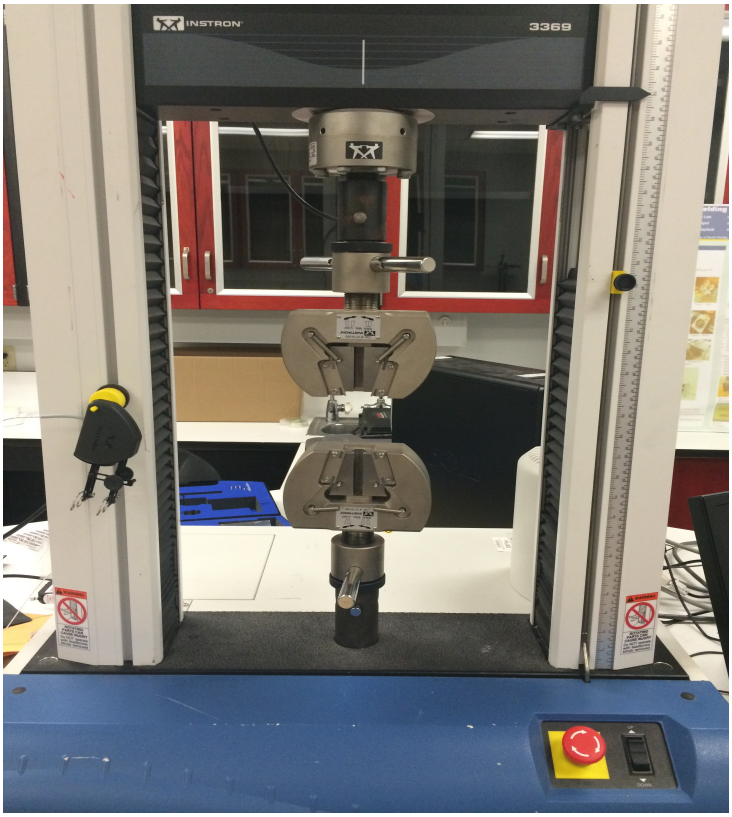

Figure 24. Instron tensile tester used in this study

3.2 Microstructure

Back scattered electron (BSE) images of both the longitudinal and transverse direction were taken. Grain size is approximately uniform throughout with roughly equiaxed grains seen in the transverse plane, and elongated grains in the longitudinal plane, typical of wrought material (Figure 25 and 26). White spots are β (Mg_2Si) precipitates.

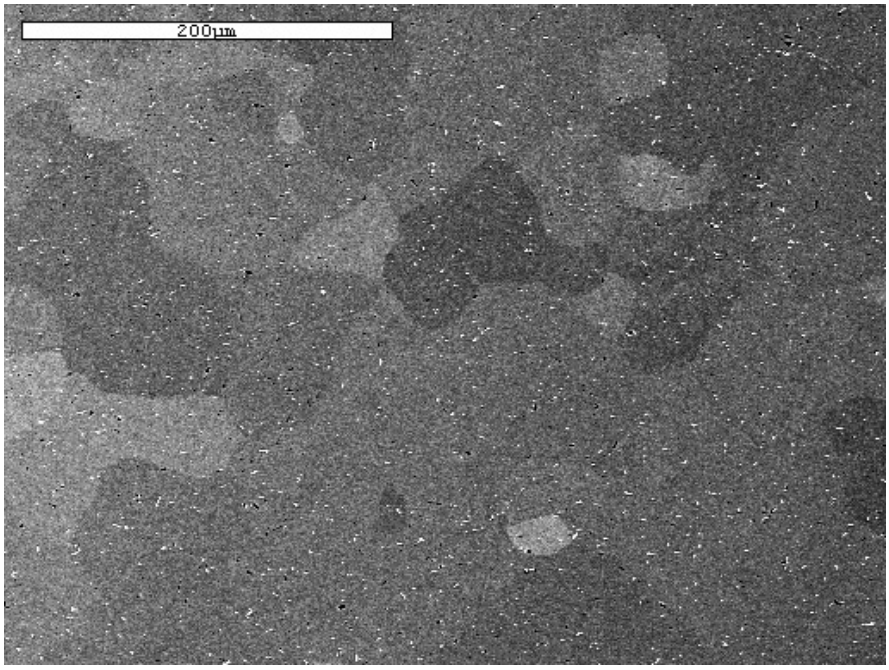

Figure 25. BSE image of transverse plane in AA 6061-T6. White spots are β (Mg_2Si) precipitates. Contrast in grey regions is due to electron channeling from grain orientation

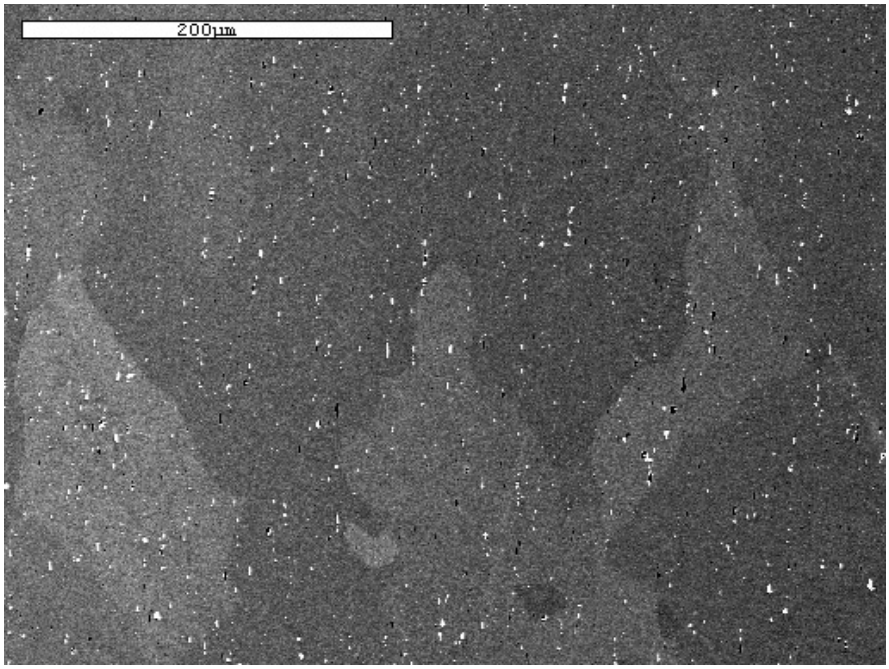

Figure 26. BSE image of longitudinal direction in AA 6061-T6. White spots are β (Mg_2Si) precipitates. Contrast in grey regions is due to electron channeling from grain orientation

3.3 Preliminary Corrosion Experiment

A small-scale corrosion test was performed to verify assumptions about resulting pit sizes and to obtain preliminary data to better design experiments. Five 300 mL 3.5% NaCl solutions were prepared using 99.5% purity NaCl from Fisher Scientific. Two solutions were prepared at pH 2, two at pH 4 and one at neutral pH (Table 5). The pH of the solutions was adjusted using 6 M hydrochloric acid (HCl). The HCl was diluted from stock HCl from Fisher Scientific.

Specimens were corroded for two different durations. Two fatigue specimens were allowed to corrode for 12 hours at pH 2 and pH 4, while the other two fatigue specimens were allowed to corrode for 24 hours at pH 2 and pH 4. The pH neutral specimen was corroded for 3 days. The samples were cleaned in a bath of 5% HNO_3 for 10 s, followed by a water rinse and sonication in ethanol to remove the corrosion products from the surfaces. A Fatigue Dynamics RBF-200 rotational fatigue tester was used to fatigue the specimens (Figure 27). The samples were then analyzed through the use of a JEOL 6400 Scanning Electron Microscope for verification that pitting and fatigue due to surface flaws had occurred (Figure 28 and Figure 29).

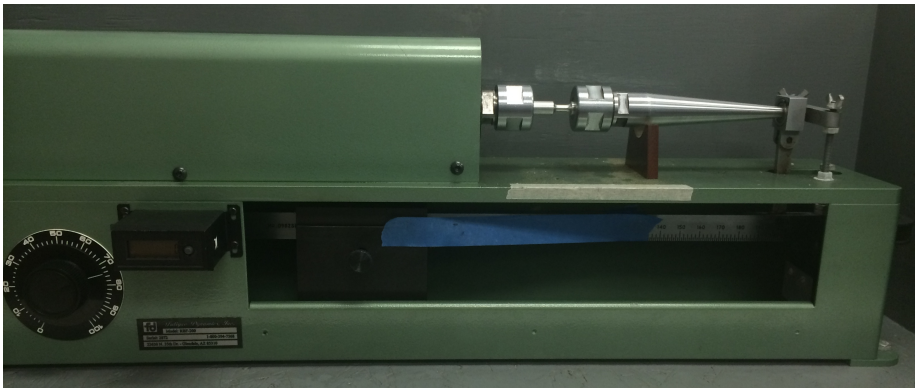

Figure 27: Rotating beam fatigue tester used in this study

Table 5. Preliminary corrosion bath formulations

	Solution				
	1	2	3	4	5
pH	2	2	4	4	neutral
Time of corrosion (hrs)	12	24	12	24	72
Amount of NaCl (g)	10.39	10.39	10.5	10.5	10.5
Chloride from acid (g)	0.106	0.106	0.001	0.001	N/A
Total amount (g)	10.5	10.5	10.5	10.5	10.5
Percent weight Cl^- (%)	3.5	3.5	3.5	3.5	3.5

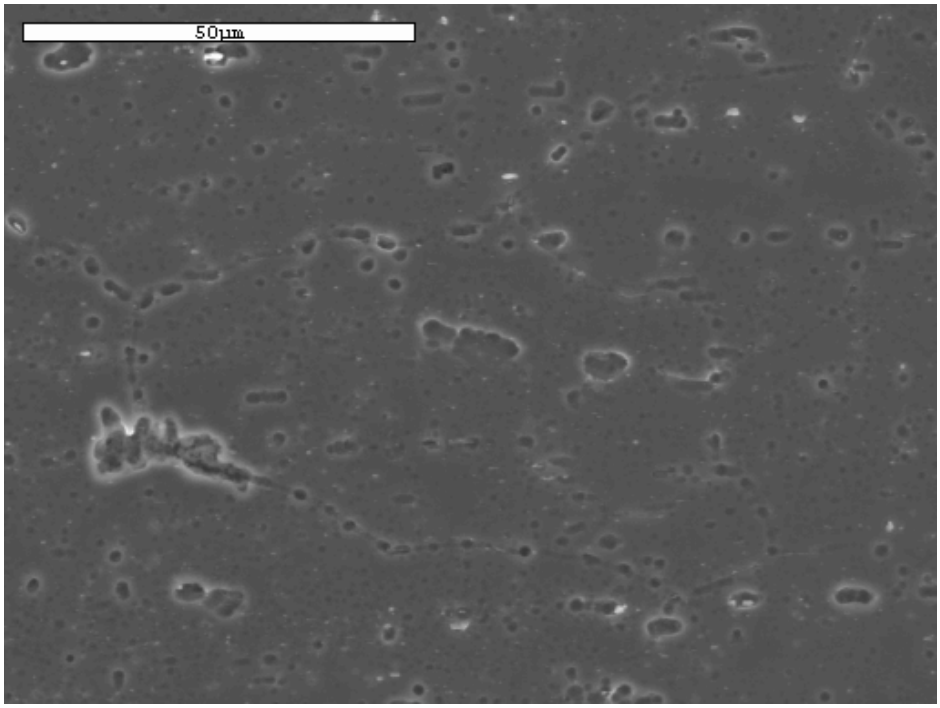

Figure 28. SEM micrograph of preliminary corrosion test of AA 6061-T6, pH 2, 24 hrs indicating localized pitting as suggested by Cavanaugh [77] for low pH.

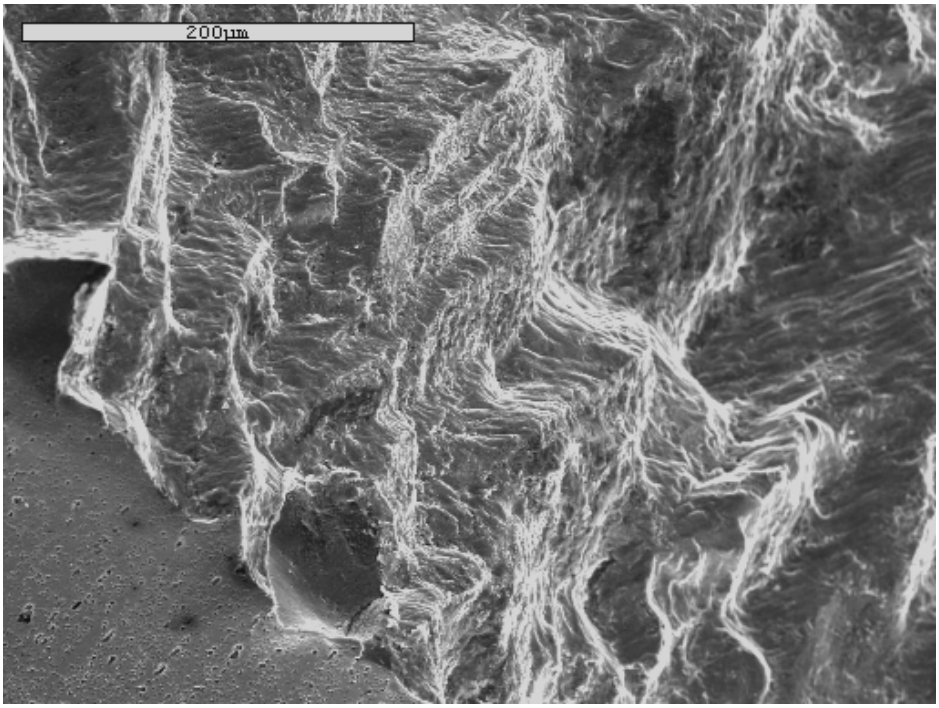

Figure 29. Fatigue of corroded AA 6061-T6 specimen, pH 2, 24 hrs. The sample was tested at nominal stress of 230 MPa for N_f = 21200 cycles. Used to verify surface initiation in preliminary tests

3.4 Corrosion Procedure

Two 2.5 gal solutions of pH 2, 3.5% NaCl (99.5% purity, Fisher Scientific) were made. An 11x11 grid of plastic was used to keep the samples upright and fatigue regions of the samples exposed (Figure 30). The solution was brought down to pH 2 through the use of 6 M HCl. The 6 M HCl was diluted from stock HCl (Fisher Scientific). 25 fatigue samples were corroded for 2 days, while another 25 were corroded for 24 days. Corrosion took place in a closed container, at room temperature in a non-circulating bath. Upon removal from solution, corrosion was stopped by placing the samples in a 5% HNO_3 bath for 10 seconds followed by a rinse in water and then samples were cleaned ultrasonically in ethanol.

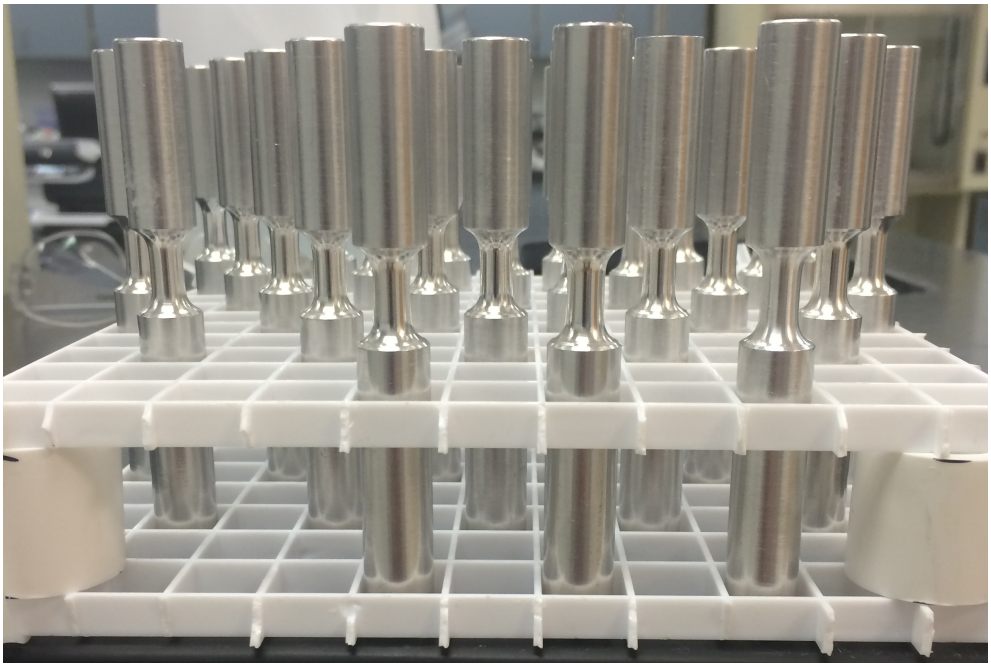

Figure 30. Sample support apparatus with AA 6061-T6 fatigue samples. Samples are spaced apart with fatigue region fully exposed to corrosion bath.

3.5 Fatigue Testing of Aluminum alloy 6061-T6 extrusions

A Fatigue Dynamics RBF-200 rotational fatigue tester was used to fatigue the specimens at 7000 rpm. The following formula was used to determine where the weight should be set in order to apply the desired load.

$$M = \frac{\pi\sigma}{32} D^3 \tag{3.1}$$

M = applied moment (lb*in)

σ = applied stress level (psi)

D = diameter of fatigue specimen (in)

Five fully reversed stress states were chosen to ensure for a better data fitting for the S-N curve (Table 4). As each sample fatigued the number of cycles to failure was recorded and the fracture surfaces were protected for fractographic analysis. An additional set of 4 polished fatigue specimens were fatigued to verify that surface corrosion was causing a

reduction in fatigue life (Table 6). After the samples had been fatigued to failure, a JEOL 6400 SEM was used to document the fracture surfaces of the fatigued specimens, and identify regions of interest.

Table 6: Table documenting specimen number, corrosion and fatigue parameters for polished, un-corroded specimens

Specimen #	Number of Days Corroded	Applied Strss (MPa)	% Yield Strengh	Moment (Nm)	# cycles to fatigue
1	0	230	90	5.37	33,300
2	0	230	90	5.43	49,500
3	0	128	50	3.02	12,049,000
4	0	128	50	3.02	11,900,300

Chapter 4: Results and discussion

4.1 Fatigue Test Results

Tables 7 and 8 present the 50 specimen numbers, the applied stress and the fatigue life data of the corroded AA 6061-T6 specimens. Table 9 presents the polished, uncorroded samples numbers, applied stress and fatigue limits. Fatigue lives were similar for unpolished and corroded samples at high stress. Fatigue lives for low stress uncorroded are longer than fatigue lives of low stress corroded samples indicating that corrosion has an effect on fatigue life.

Table 7. Fatigue life data for AA 6061-T6, 2-day corrosion, 3.5% NaCl, pH 2, fatigue samples. * denotes that the sample was removed before failure

Specimen #	Number of Days Corroded	Applied Strss (MPa)	% Yield Strengh	Moment (Nm)	# cycles to fatigue
231	2	230	90	5.30	25,800
233	2	230	90	5.37	28,600
235	2	230	90	5.37	41,300
237	2	230	90	5.30	45,900
239	2	230	90	5.37	35,900
2311	2	191	75	4.47	143,300
252	2	191	75	4.47	160,700
254	2	191	75	4.42	147,300
256	2	191	75	4.42	84,500
258	2	191	75	4.36	105,400
2510	2	153	60	3.58	371,900
271	2	153	60	3.49	392,100
273	2	153	60	3.58	550,500
275	2	153	60	3.49	345,700
277	2	153	60	3.49	360,100
279	2	128	50	2.98	1,584,700
2711	2	128	50	3.02	2,012,000
292	2	128	50	3.02	1,738,700
294	2	128	50	2.94	1,502,200
296	2	128	50	2.94	1,390,500
298	2	115	45	2.65	2,863,100
2113	2	115	45	2.68	18,706,200
2115	2	115	45	2.68	4,474,200
2117	2	115	45	2.68	33,723,300
2910	2	102	40	2.44	*38,348,700

Table 8. Fatigue life data for AA 6061-T6, 24-day corrosion, 3.5% NaCl, pH 2, fatigue samples. * denotes that the sample was removed before failure

Specimen #	Number of Days Corroded	Applied Strss (MPa)	% Yield Strengh	Moment (Nm)	# cycles to fatigue
2431	24	230	90	5.30	37,200
2433	24	230	90	5.37	30,800
2435	24	230	90	5.47	26,900
2437	24	230	90	5.30	40,500
2439	24	230	90	5.30	38,700
24311	24	191	75	4.31	132,000
2452	24	191	75	4.50	122,900
2454	24	191	75	4.50	102,300
2456	24	191	75	4.47	157,800
2458	24	191	75	4.47	96,000
24510	24	153	60	3.49	425,700
2471	24	153	60	3.53	363,000
2473	24	153	60	3.53	414,900
2475	24	153	60	3.40	612,300
2477	24	153	60	3.53	375,100
2479	24	128	50	3.05	2,546,500
24711	24	128	50	2.98	5,702,600
2492	24	128	50	2.98	1,340,700
2494	24	128	50	2.98	1,411,000
2496	24	128	50	2.98	1,207,300
24910	24	115	45	2.68	17,425,000
24113	24	115	45	2.68	1,365,300
24115	24	115	45	2.68	1,260,400
24117	24	115	45	2.65	5,048,200
2498	24	102	40	2.38	*72,368,900

Table 9. Fatigue life data for AA 6061-T6, polished fatigue samples

Specimen #	Number of Days Corroded	Applied Strss (MPa)	% Yield Strengh	Moment (Nm)	# cycles to fatigue
1	0	230	90	5.37	33,300
2	0	230	90	5.43	49,500
3	0	128	50	3.02	12,049,000
4	0	128	50	3.02	11,900,300

4.2 S-N curves

The numbers of cycles to failure for 2-day and 24-day corroded specimens were plotted against the maximum stress to produce S-N curves with run outs being indicated by solid data markers with arrows (Figures 31-33). A run out is the term used for intentional sample removal prior to failure, after excessively high cycles (greater then 10^7 cycles). After that many cycles it is assumed that the sample may exhibit unpredictably long fatigue life and while noted as a run out, is not used in the calculation of S-N curve. The curves were fitted using Basquin's Law [15]. The Basquin exponents for 2-day and 24-day corrosion specimens were determined to be 0.123, and 0.128 respectively. These values match closely to the one (0.130) reported by Tiryakioğlu et al. [18] for forged AA 6061-T6 in rotational fatigue tests conducted at fully reversed stress. The experimental values were verified through linear regression (Table 10). It should be noted that 2 samples were removed from the analysis for the 24 day corrosion due to large manufacturing defects.

Some observations from the data include; at high stress (230 MPa) the 2-day corrosion samples are observed to fatigue before the 24-day corrosion samples. Additionally, scatter in the data is observed at 128 MPa for 24-day corrosion and 115 MPa for 2-day corrosion. Both deviations are believed to be due to different fatigue initiation mechanisms and will be discussed in forthcoming sections. Run outs occurred at 102 MPa and while plotted on the S-N curve, were not used for the Basquin equation. Run outs were used in the Weibull analysis.

Table 10. Linear regression of S-N curve data. LCL refers to lower confidence limit, UCL refers to upper confidence limit

	2-day		24-day	
Basquin Coefficient	-0.123		-0.128	
95% LCL and UCL	-0.140	-0.106	-0.143	-0.112
Constant, C	844		787	
95% LCL and UCL	844	1028	631	982

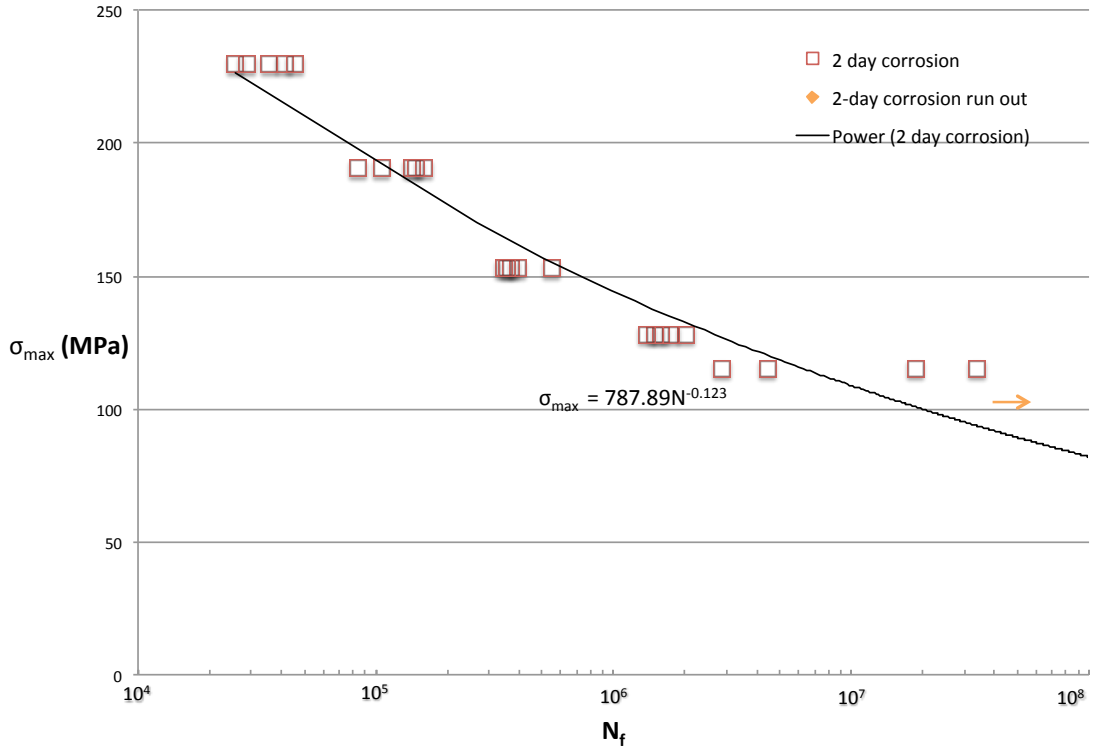

Figure 31. S-N curve for AA 6061-T6 specimens corroded for 2-days in 3.5% NaCl at pH 2

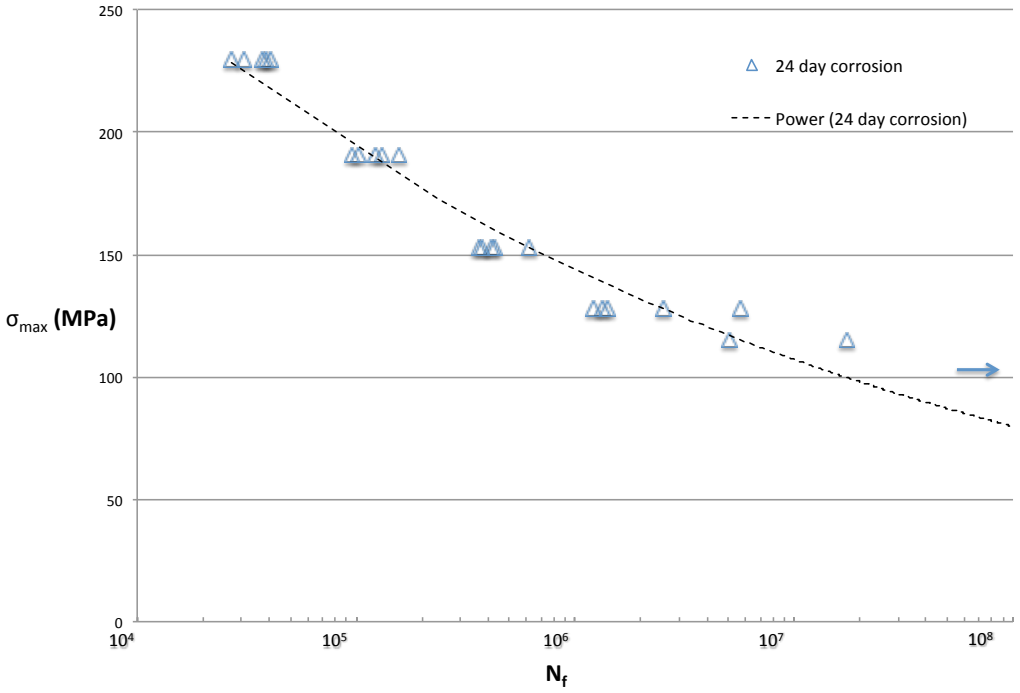

Figure 32. S-N curve for AA 6061-T6 specimens corroded for 24-days in 3.5% NaCl at pH 2

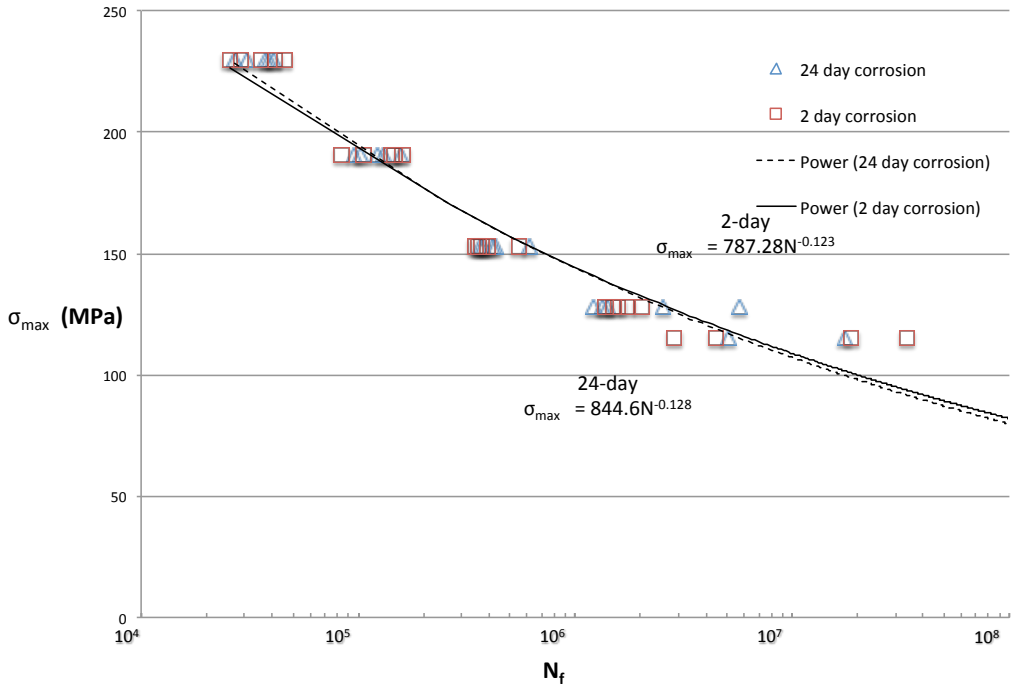

Figure 33. S-N curve of both 2-day and 24-day specimens shown together for direct comparison. Run outs not shown

4.3 Micrographs

4.3.1 Pit Cross Sections

Cross sectional micrographs of both 2-day and 24-day corroded specimens were prepared by traditional metallographic polishing. This was done to observe the pit morphology in cross section before the samples were fatigued. The 2-day corroded specimens exhibit small diameter pit openings around 1-2 μm. Additionally, the 2-day corroded surfaces appear unaffected by general corrosion. The 24-day corroded specimens have broad, scalloped pits with coincident and overlapping borders. The pits also appear shallower then expected if the power law discussed in section 2.3.2 is followed, allowing for the conclusion that more aggressive general corrosion took place in 24-day specimens. It can also be observed that a layer of scale had been deposited on the 24-day corrosion specimens. Representative micrographs are shown in Figures 34-37.

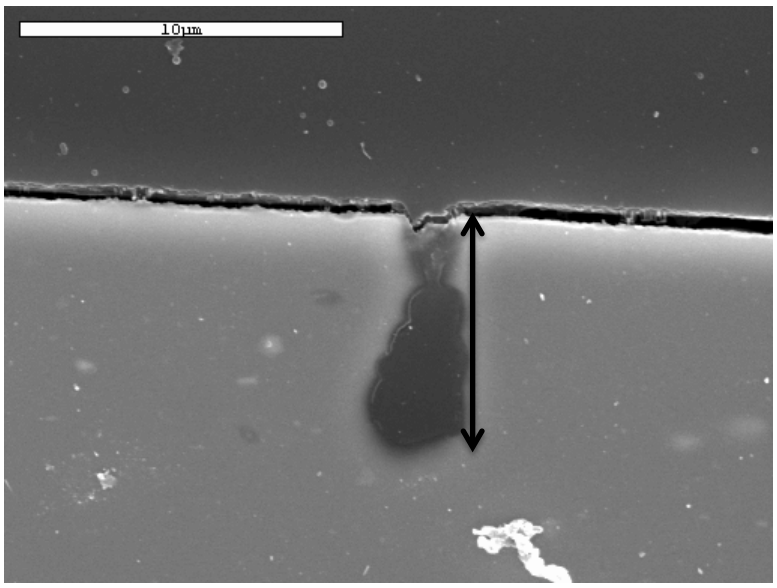

Figure 34. SEM image of AA 6061-T6, 2-day corroded cross-section. The double pointed arrow shows the depth of the flaw at approximately 10 μm or less. The lighter region indicates a different pit morphology.

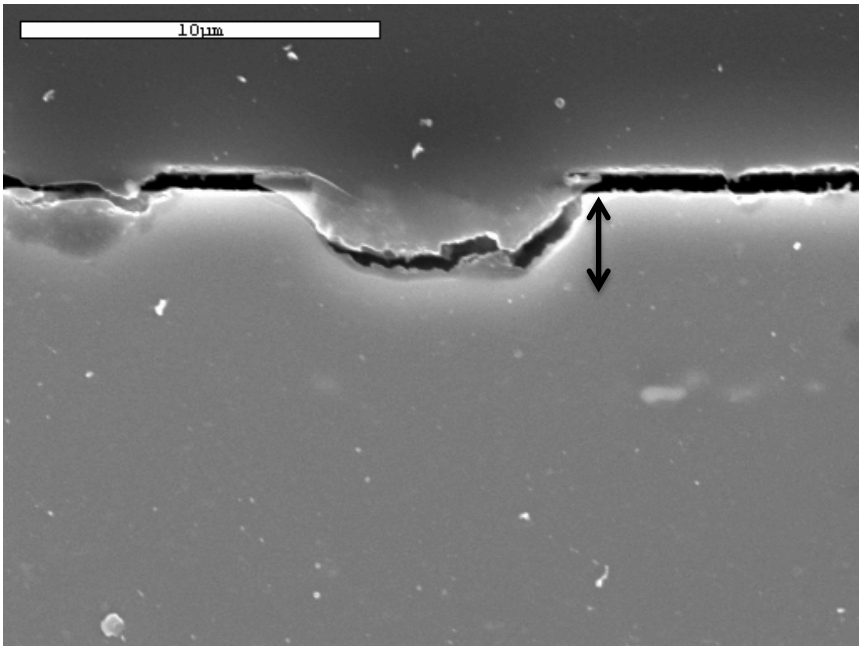

Figure 35. SEM micrograph of AA 6061-T6, 2-day, 3.5% NaCl, pH 2, corrosion cross-section. The double pointed arrow shows Pit depth appears on the order of 5 µm or less. Small flaws along the surface can be observed.

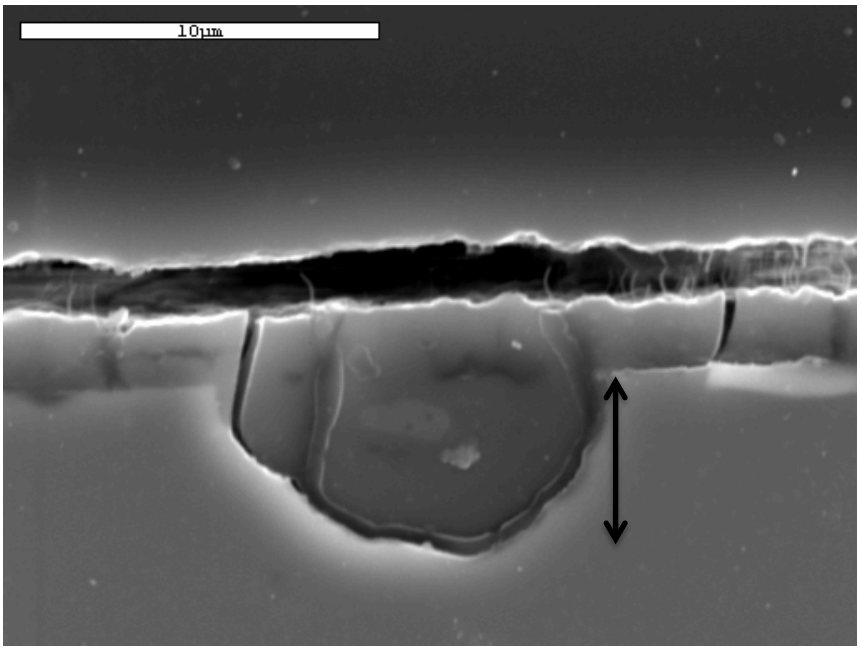

Figure 36. SEM micrograph of AA 6061-T6, 24-day, 3.5% NaCl, pH 2, corrosion cross-section. A scale layer of constant thickness is observed adhered to the specimen. The double pointed arrow shows the depth of the flaw on the order of 10 µm or less.

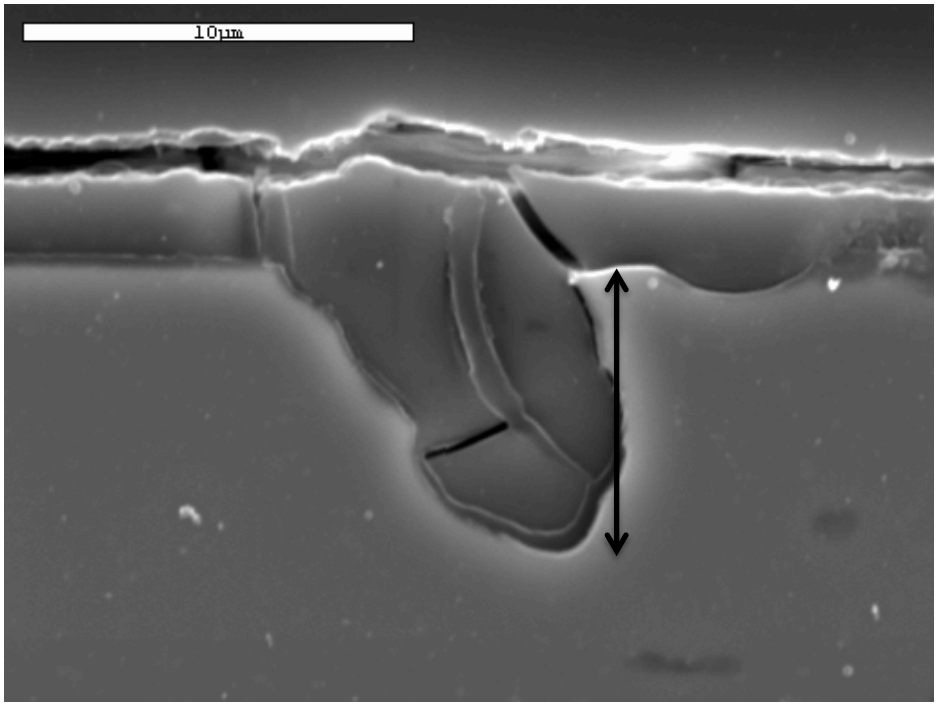

Figure 37. SEM micrograph of AA 6061-T6, 24-day, 3.5% NaCl, pH 2, corrosion cross-section. A scale layer of constant thickness is observed adhered to the specimen. The double pointed arrow shows the depth of the flaw on the order of 10 µm or less.

4.3.2 Fractographs

Fractographs are broken up into four categories; high stress 2-day corroded, low stress 2 day corroded, high stress 24-day corroded and low stress 24-day corroded. This was done in order to compare the mechanisms occurring within the same corrosion conditions.

4.3.2.1 High Stress, 2-Day Corroded

It was possible to identify regions of fatigue initiation from the orientation of striation relative to the flaw. The broad striae, which are indicative of high stress fatigue, are observed perpendicular to the perimeter of the cracked grain. Figure 38 demonstrates that striae are found leading to the surface of the specimen except in the area where the grain cracked as indicated by the arrows.

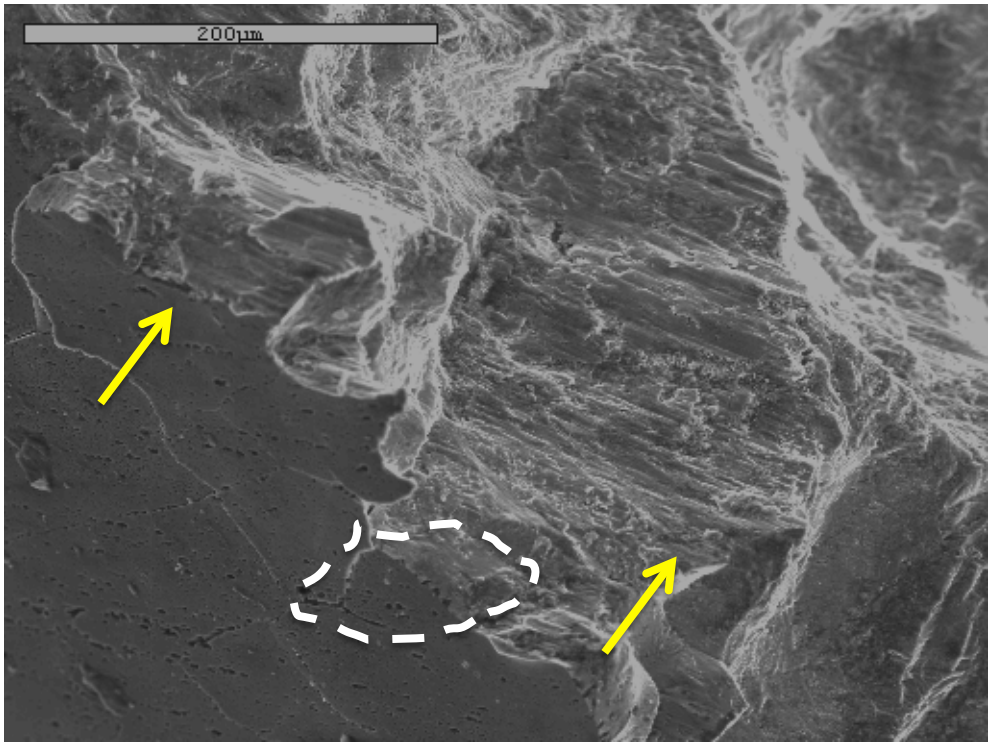

Figure 38. SEM micrograph of AA 6061-T6, 2 day corrosion, σ = 230 MPa, N_f = 25800 cycles, Sample # 231. Sample was tilted in the SEM to bring the cylindrical sample surface into view

Pitting along the exposed portion of the grain boundary is shown in Figure 39, a higher magnification of Figure 38. There are 3 pits within close proximity of each along the exposed face, possibly a region resulting in high stress intensity. The flat surface of the exposed grain is believed to be due to grain boundary cracking. In the fractures' surfaces of the 2-day samples, grain boundary decohesion (GBD) is believed to have occurred (Figure 38 and Figure 39). It is believed that the dislocation pile up at the grain boundary would cause the grain boundary to become brittle and separate. Once separation occurs, the resulting flaw should be sufficiently large to serve as a fatigue initiation site and crack propagation will occur, ultimately leading to fatigue failure.

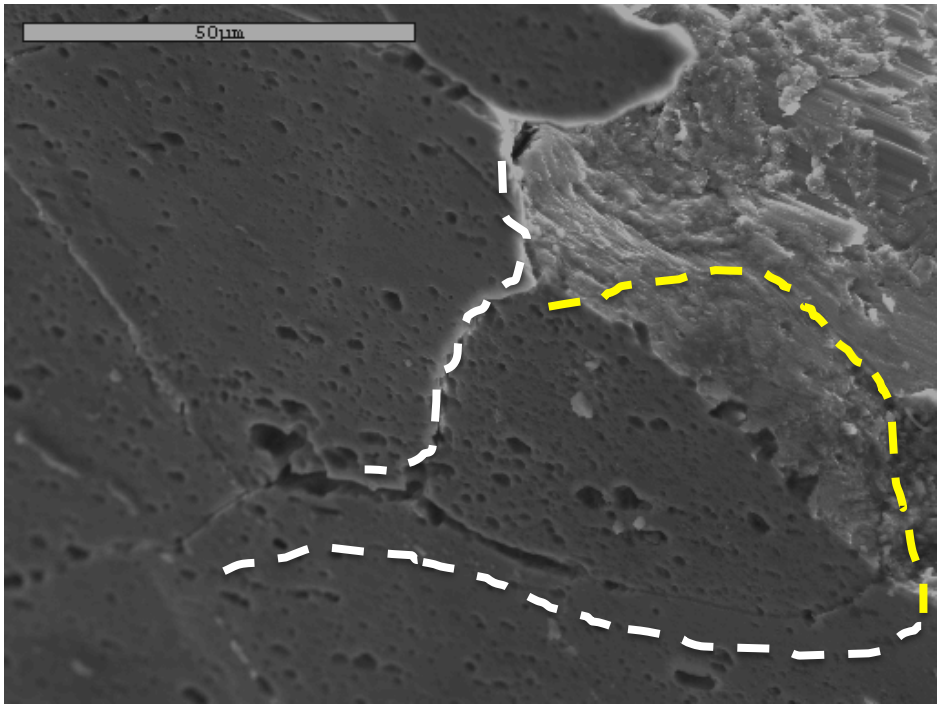

Figure 39. SEM image of AA 6061-T6, 2 day corrosion, σ = 230 MPa, N_f = 25800 cycles, Sample # 231. Tilted off axis to show the cylindrical surface of specimen. Dashed white is shown adjacent pitted boundaries. Dashed yellow line indicates the start of region II fatigue crack propagation

4.3.2.2 Low Stress, 2-Day Corroded

The striations emanating from a heavily flawed surface region (Figure 40a) are an indication that fatigue initiation/propagation occurred at that edge. Striations at low stress were observed to be finer and closer together (Figure 40b). Much like for high stress, GBD was observed in 2-day corroded fatigue specimens at low stress (128 MPa). It can be seen that the area of GBD is much larger in low stress 2-day corroded specimens (Figure 40a) then in the high stress 2-day corroded specimens (Figure 39). This probably occurs because the flaw size for initiation needs to be larger due to the lower applied stress requiring the formation of a larger flaw at the grain boundary.

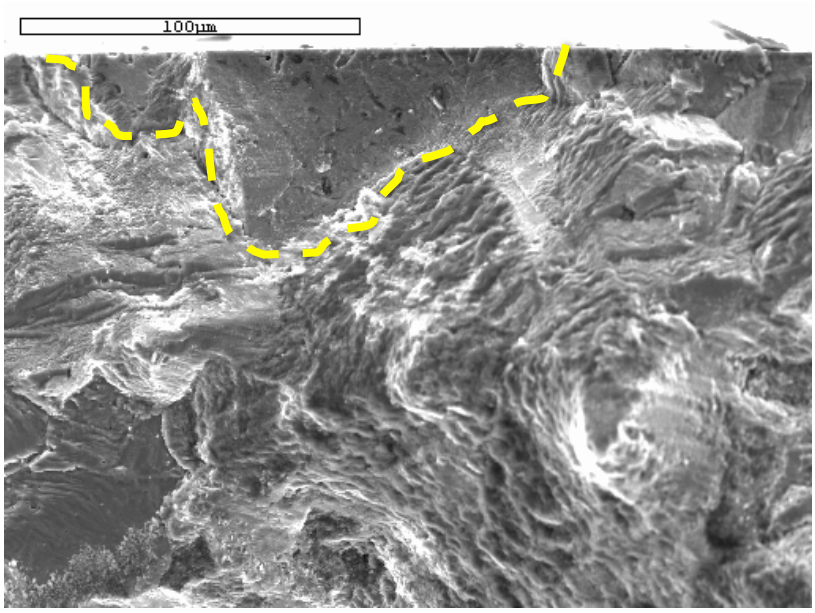

(a)

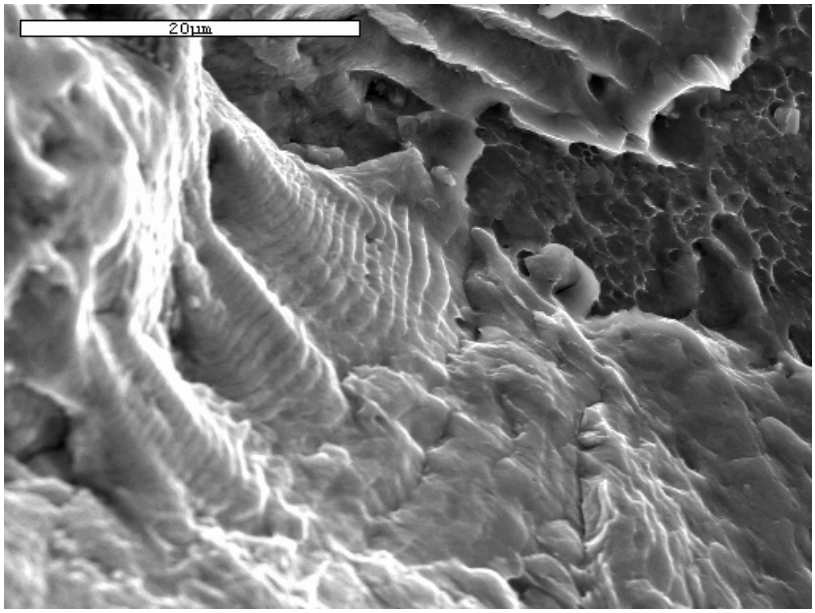

(b)

Figure 40. SEM image of AA 6061-T6, 2 day corrosion, σ = 128 MPa, N_f = 2012000 cycles, Sample # 2711. a) indicates region of GBD b) shows formation of fine structured striae on a different region of the same specimen.

4.3.2.3 High Stress, 24-Day Corroded

In the 24-day corroded specimens, a metal oxide scale was observed on the cylindrical surface of the fatigue specimen that is likely Al_2O_3 (Figure 41 and 42). From regions where scale had spalled, it was observed that the specimen beneath the scale is also heavily pitted. The scale appears heavily discontinuous, and non-adherent, therefore, it can be inferred that the scale does not impart any structural integrity to the system, and should play no role in fatigue behavior

Figure 41 shows striation indicating that crack propagation occurred. It is suggested by the orientation of striae that the heavily pitted region shown in Figure 41 (yellow dashed) was a region of fatigue initiation. Below the yellow dotted region, the striae are perpendicular to the flaw. The multiple observed orientations of striations are likely due to the rotational fatigue testing and multiple fatigue initiation sites.

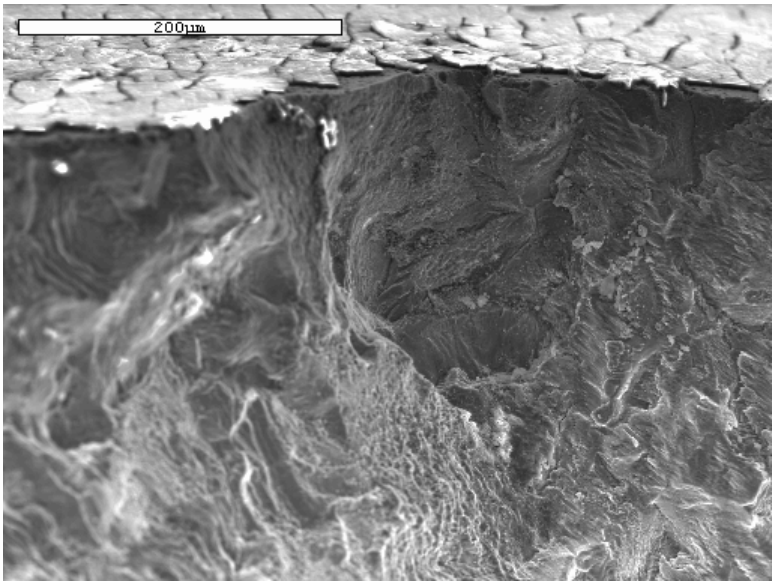

Figure 41. SEM image of AA 6061-T6, 24 day corrosion, σ = 230 MPa, N_f = 30800 cycles, Sample # 2433. Note the segmented surface scale which appears as the lighter region near the top of the fractograph. Also note the small dark pit near the center of the top of the fractograph, which will be presented in higher magnification in Figure 42.

Based on microscopy, it was determined that samples corroded for 24-days and fatigued at high stress (230 MPa), failed due to corrosion flaws that were large enough for fatigue crack propagation to occur directly from the corrosion pit border (ΔK_{th} sufficiently large). In Figure 42, the flawed region is approximately 50 μm in diameter. That is approximately the same size as the flat grain surface observed in Figure 39. This further supports a mechanism for a common flaw size necessary for fatigue initiation.

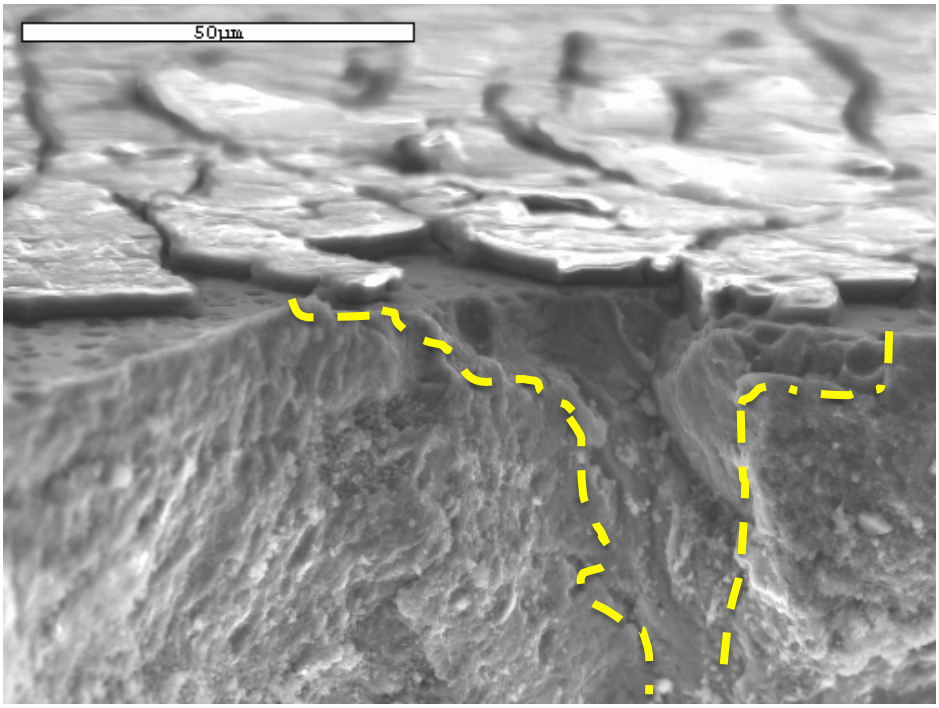

Figure 42. SEM image of AA 6061-T6, 24 day corrosion, σ = 230 MPa, N_f = 30800 cycles, Sample # 2433, as described in Figure 41.

4.3.2.4 Low Stress, 24-Day Corroded

The scatter that was observed at low stress in the fatigue data (S-N curves) for the 24-day corroded samples prompted a more detailed analysis at the fracture surfaces to explain the scatter in fatigue life data. Shown in Figure 43 are fatigue striations heading directly

from a scalloped surface flaw. The flaw is smaller than most observed in this study at less than 10 μm across and less than 10 μm deep. However, it appears to serve as an initiation site as the striations indicate the fatigue propagated from this flaw.

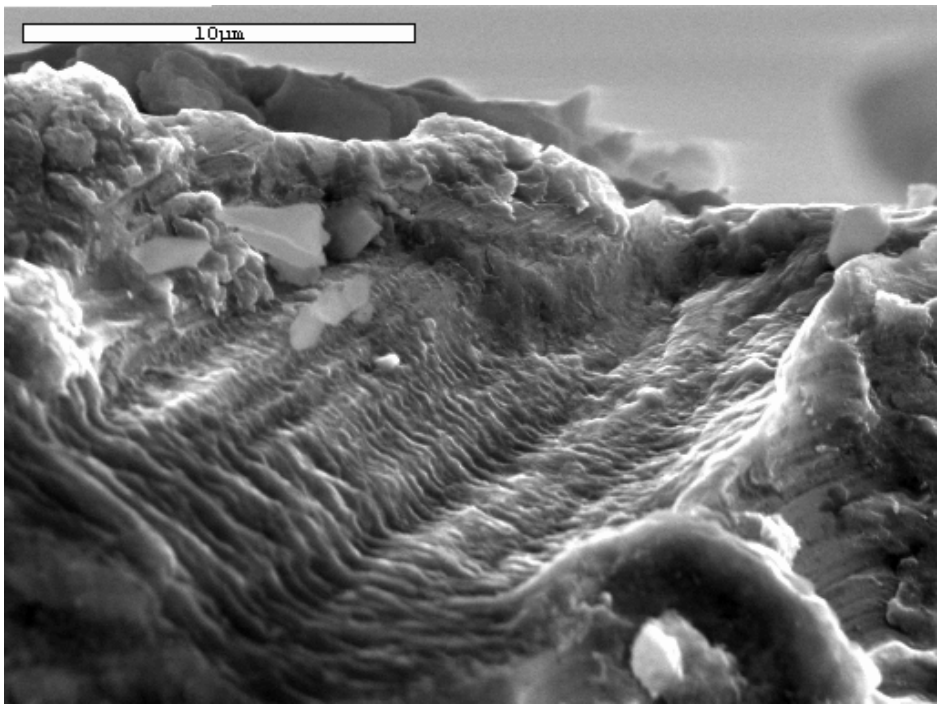

Figure 43. SEM image of AA 6061-T6, 24 day corrosion, σ = 128 MPa, N_f =1411000 cycles, Loc # 94. Notice directionality back to a surface flaw

For the 24-day corroded samples, multiple smaller initiation sites and scatter in flaw size are probable reasons for variation in fatigue initiation, leading to the scatter in the fatigue data [80].

4.3.2.5 Ductile Failure

Region III fatigue crack growth was observed as a region of ductile failure in all specimens. Representative micrographs of ductile failure in 2-day and 24-day corroded specimens are presented in Figure 44 and Figure 45.

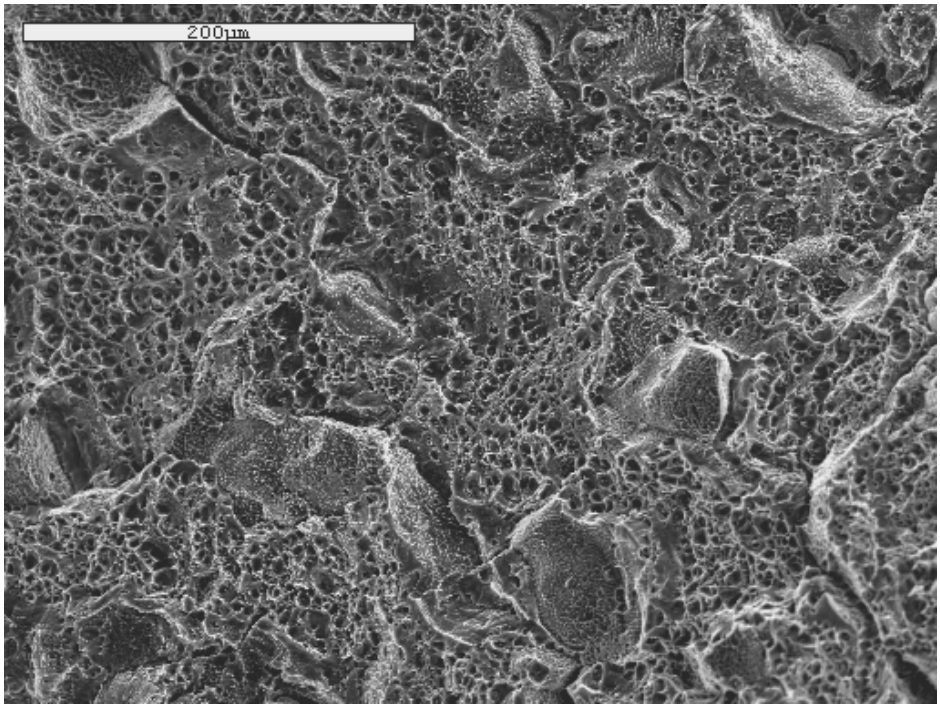

Figure 44. SEM image of AA 6061-T6, 2 day corrosion, σ = 230 MPa, N_f = 45900 cycles, Sample # 237. Region of ductile failure.

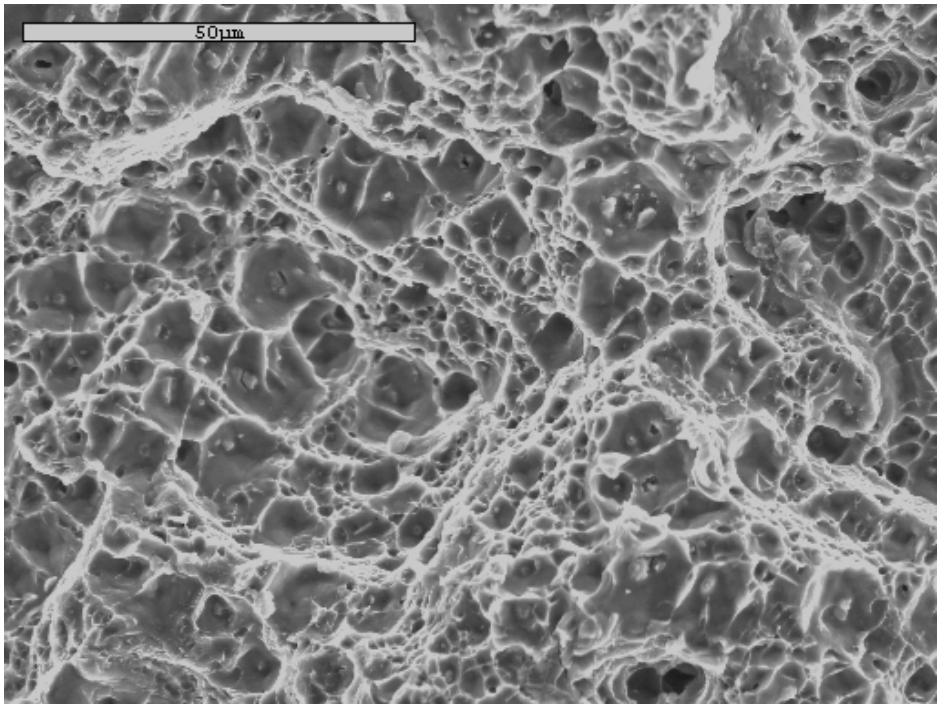

Figure 45. SEM image of AA 6061-T6, 24 day corrosion, σ = 230 MPa, N_f = 30800 cycles, Sample # 2433. Region of ductile failure.

4.4 Weibull Analysis

4.4.1 Weibull plots of 2-day and 24-day corrosion

The fatigue life data were analyzed to determine if a Weibull distribution could be applied. The fatigue data were normalized to 191 MPa in order to eliminate any error incurred due to the applied stress. Equivalent fatigue lives were calculated for the different stress levels using the following formula:

$$N_{f(2)} = N_{f(1)} \left(\frac{\sigma_1}{\sigma_2}\right)^{\frac{1}{k}} \tag{4.1}$$

$N_{f(2)}$ = equivalent fatigue life

$N_{f(1)}$ = original fatigue life

σ_1 = original stress

σ_2 = equivalent stress

k = Basquin coefficient

The Weibull probability density functions (PDF) of fatigue data for both 2-day and 24-day corrosion specimens are shown in Figure 46 and Figure 47. Analysis of the data was initially performed using a two-parameter Weibull distribution in Minitab. It was determined that a three-parameter Weibull distribution was better suited to explain the data. The goodness-of-fit of the estimated paramters was tested by using the Anderson-Darling (AD) statistic, A^2 [82]:

$$A^2 = -n - \frac{1}{n}\sum_{i=1}^{n}\left[(2i-1)ln\left(P\left(N_f\right)_i\right) + \ln\left(1 - P\left(N_{f+1-i}\right)\right)\right] \tag{4.2}$$

Where $P(N_f)_i$ = the cummulative probability for each data point. A small A^2 value provides a higher confidence that the data follow the hypothesized distribtion of a 3-parameter Weibull. Additionally, the hypothesis is rejected when the AD value is less than 0.05. This value typically corresponds to a Type 1 error (α). Table 11 shows the threshold values for both 2-day and 24-day corroded specimens, scale factor, shape factor, A^2 , and the critical value below which A^2 cannot be rejected. These values support the conclusion that the data are represented by a three-parameter Weibull distribution and the hypothesis could not be rejected.

Table 11. Summary of Weibull parameters for 2-day and 24-day corroded specimens, AD critical values taken from [83]

	2-day corroded	24-day corroded
Number of samples	25	23
Threshold Value, N_t	45248	52080
Scale Factor, N_o	80748	98356
Shape Parameter, *m*	0.913	0.822
A^2	0.400	0.128
$A^2_{0.05}$	0.592	0.587

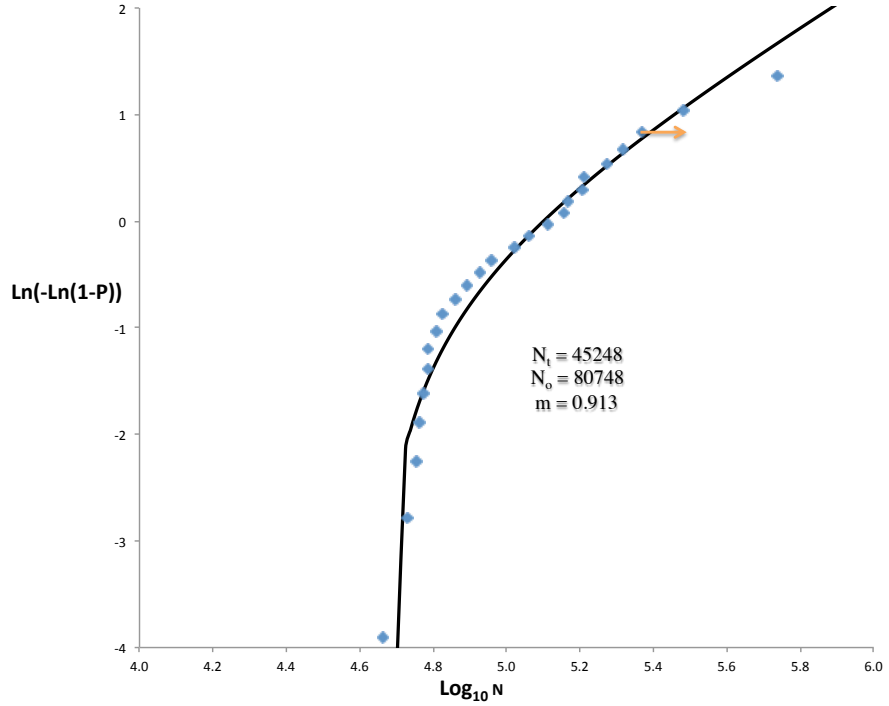

Figure 46. Three-parameter Weibull distribution for 2-day corrosion AA 6061-T6 samples. Arrow indicates sample run out

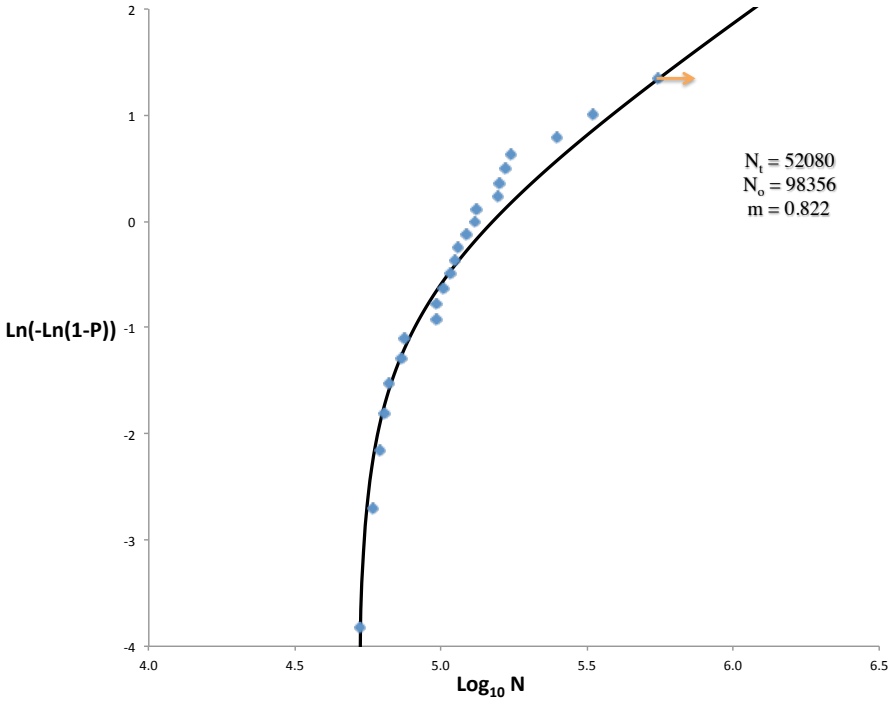

Figure 47. Three-parameter Weibull distribution for 24-day corrosion AA 6061-T6 samples. Arrow indicates sample run out.

Another representation of the effect of corrosion on the fatigue life AA 6061-T6 in 3.5% NaCl at pH 2 can been seen in the probability density functions of the two different corrosion times (Figure 48). The PDF is defined as:

$$f = \frac{dP}{d\sigma} \tag{4.3}$$

For the Weibull distribution, f is expressed as:

$$f = \frac{m}{\sigma_0}\left(\frac{\sigma-\sigma_t}{\sigma_0}\right)^{m-1} \exp\left[-\left(\frac{\sigma-\sigma_t}{\sigma_0}\right)^{m}\right] \tag{4.3a}$$

It can be seen that exposure to 3.5% NaCl at pH 2 for 2-days causes a 12.2% drop in threshold fatigue life. Therefore, it has been demonstrated that the longer exposure time serves to shallow out the flaws and provide for a more even distribution of stress along the flaw surface.

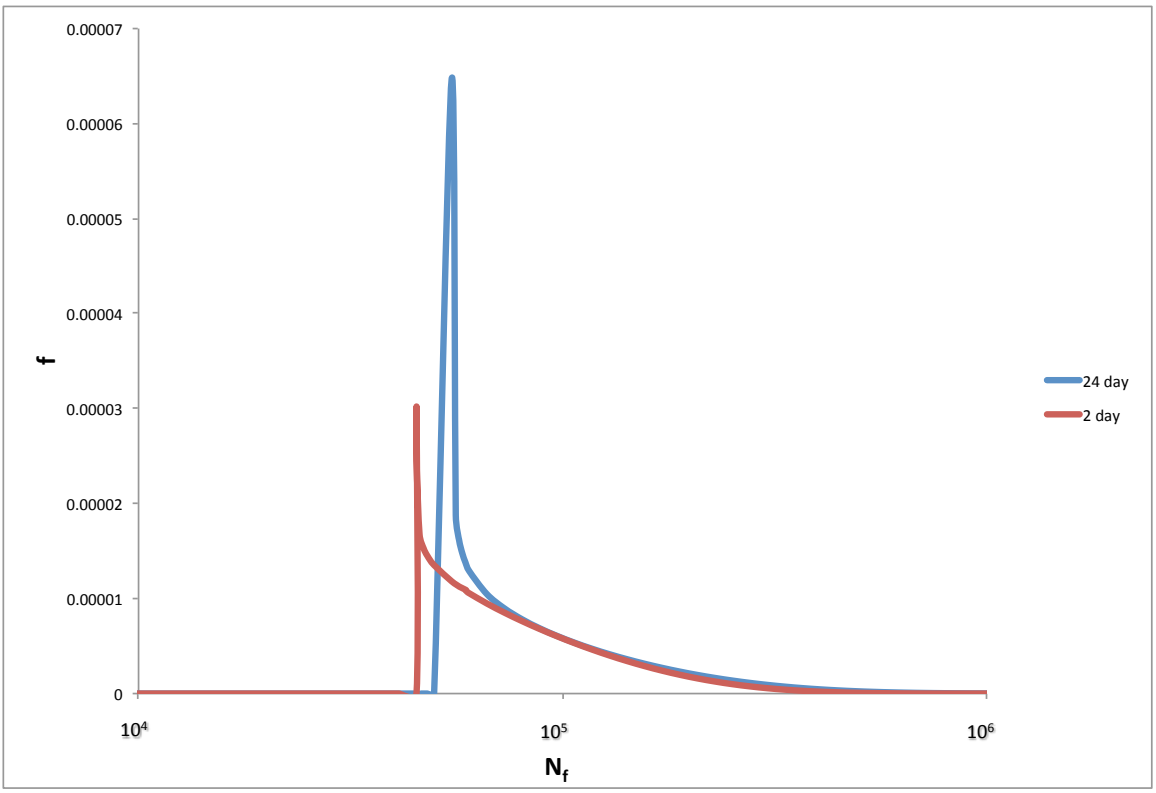

Figure 48. Probability density functions for both 2-day and 24-day corrosion of AA 6061-T6 in 3.5% NaCl at pH 2.

4.4.2 Pit Size Distribution

The observation that a three-parameter Weibull distribution is a good representation of the data allows for some discussion on the flaw size distribution in both 2-day and 24 day corroded AA 6061-T6. The result that AA 6061-T6 exposed to the previously described corrosive environment follows a three-parameter Weibull distribution and has a threshold fatigue life, means that sufficiently small flaws were created. A higher threshold value for 24-day corrosion when compared to 2-day corrosion would mean that an increase in exposure time yields a widening of the size distribution of the largest flaw (Figure 49). It also means that the flaw geometry of the 2-day corroded samples was more deleterious than the 24-day flaw geometry.

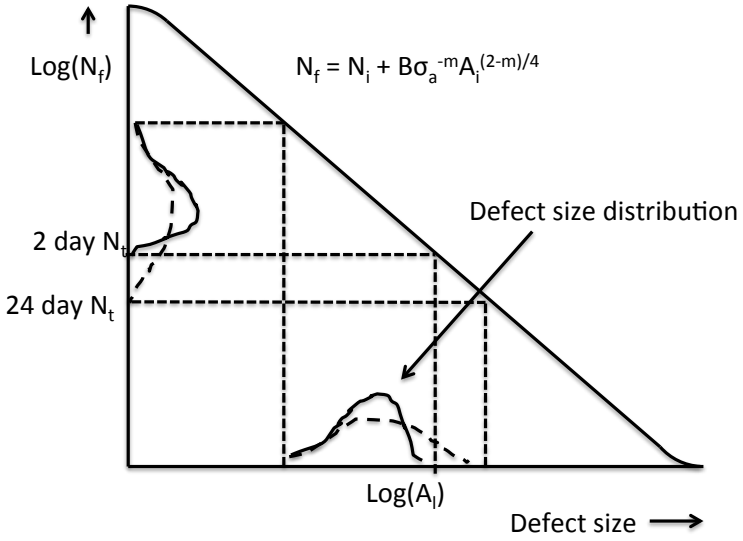

Figure 49. Schematic illustration of the effect of defect size distribution on the distribution of fatigue life (N_f). The threshold value N_t is also indicated.

4.5 Observed Scatter in Data and Variation in Fatigue Life

Scatter is observed at the lower stress levels (115 MPa and 128 MPa) for both 2-day and 24-day corroded specimens respectively. For low stress, 2-day corroded specimens (115 MPa), the scatter observed indicates that varied ΔK is resulting in variation of fatigue crack initiation. This variation is due to small, sharp pits, which lead to grain boundary decohesion. The resulting exposed grain boundary serves as the fatigue initiating flaw. In contrast, it was observed in the 24-day corroded samples that fatigue initiated at the edge of the corrosion pits themselves. It has been shown by Dolley et al. [80] that in pre-corroded AA 2024-T3, the corrosion pits serve as the point of fatigue crack initiation and growth. The scatter in the data is a result of the variation in pit size and morphology, both of which have an exaggerated effect at low stress. Fatigue initiation from the pit edge indicates a different fatigue crack initiation mechanism then the one observed in the 2-day corroded specimens.

A slight decrease in fatigue life (S-N curves, Figure 33) can be observed at high stress in 2-day corroded specimens when compared to 24-day corroded specimens. For 2-day corroded specimens, the shorter fatigue life at higher stress indicates that ΔK is large enough to cause immediate grain boundary decohesion resulting in faster fatigue crack initiation when compared to 24-day corroded specimens. It is assumed that a fractured grain boundary, presents a crack of nearly zero crack tip radius, thus exacerbating stress intensity, and providing a more potent fatigue initiation site. A visual comparison of fatigue crack initiating flaws is shown in Figure 50.

The fatigue life of a material is marked by three distinct phases; initiation, propagation and final fracture. All three phases require a crack growth mechanism that is reliant upon the stress intensity factor ΔK, which is a function of flaw geometry, the applied stress and the size of the crack. Within each of these regions, the factors that define ΔK behave differently, such that microstructural features and flaw geometry will dominate the initiation region behavior, but have no effect on the propagation region behavior.

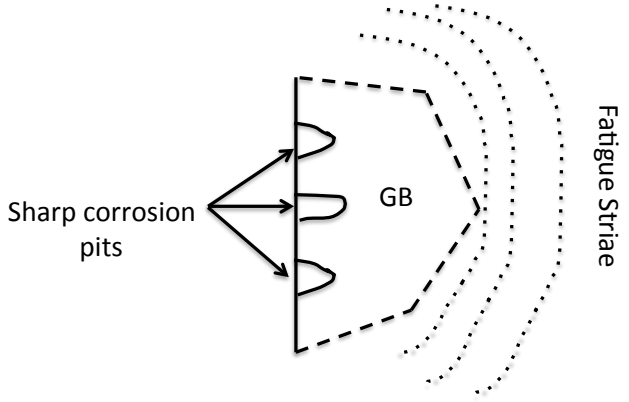

(a)

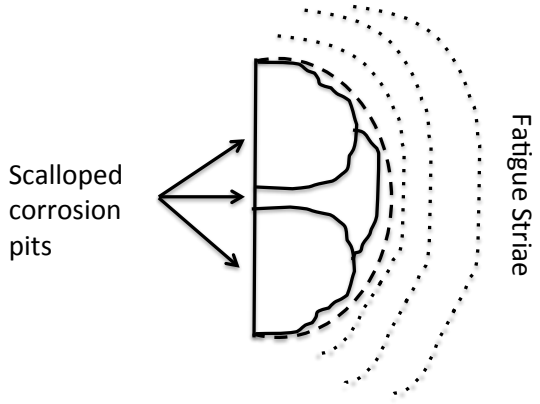

(b)

Figure 50. a) 2-day corroded specimen fatigue crack initiation due to flaw created due to grain boundary cracking. b) 24-day corroded specimen fatigue crack initiation due to corrosion flaws

Since the material and microstructure can be assumed constant in this study, there can be no variation or scatter in fatigue life from the propagation phase or final fracture. It is therefore deduced, that variation and scatter in the fatigue life data is the result of differing mechanisms in initiation which is supported by the mechanism illustrated in Figure 50.

Chapter 5: Conclusions and Future Work

From the comparison of fractographs and statistical analysis a greater understanding of the variation in micromechanisms of fatigue initiation and propagation among corroded specimens was established. Figure 51 shows a flow chart that summarizes the proposed phenomenological process involved in the fatigue of corroded AA 6061-T6 in 3.5% NaCl, pH 2 for 2-days and 24-days. Green boxes indicate fatigue crack initiation (region I), yellow boxes indicate fatigue crack propagation (region II), and red boxes indicate failure (region III).

It was determined that corrosion has a negative effect on the fatigue life of AA 6061-T6 no matter the length of exposure. It was also determined that the different lengths of corrosion yield different fatigue initiation mechanisms. Operating under the assumption that any surface degradation should negatively impact fatigue life, the broad results of this study are not revolutionary. What is of special note from this study is the effect that small changes in the morphology of surface flaws have on fatigue initiation mechanisms, thereby affecting the shape of the S-N curves and the Basquin exponent. Considering the number and variability of parameters at play in corrosive attack, designers should be keenly aware of the impact the slight changes in environment may have on predicted design lives.

It should be noted that selection of variable parameters of corrosion media, pH, temperature, etc. would produce surface flaws of varying characteristics. Additionally, many authors apply Weibull statistics to deduce exact pit size distributions instead of

relating pit size distribution to fatigue data. As such, the realm of future work regarding corroded AA 6061-T6 is vast.

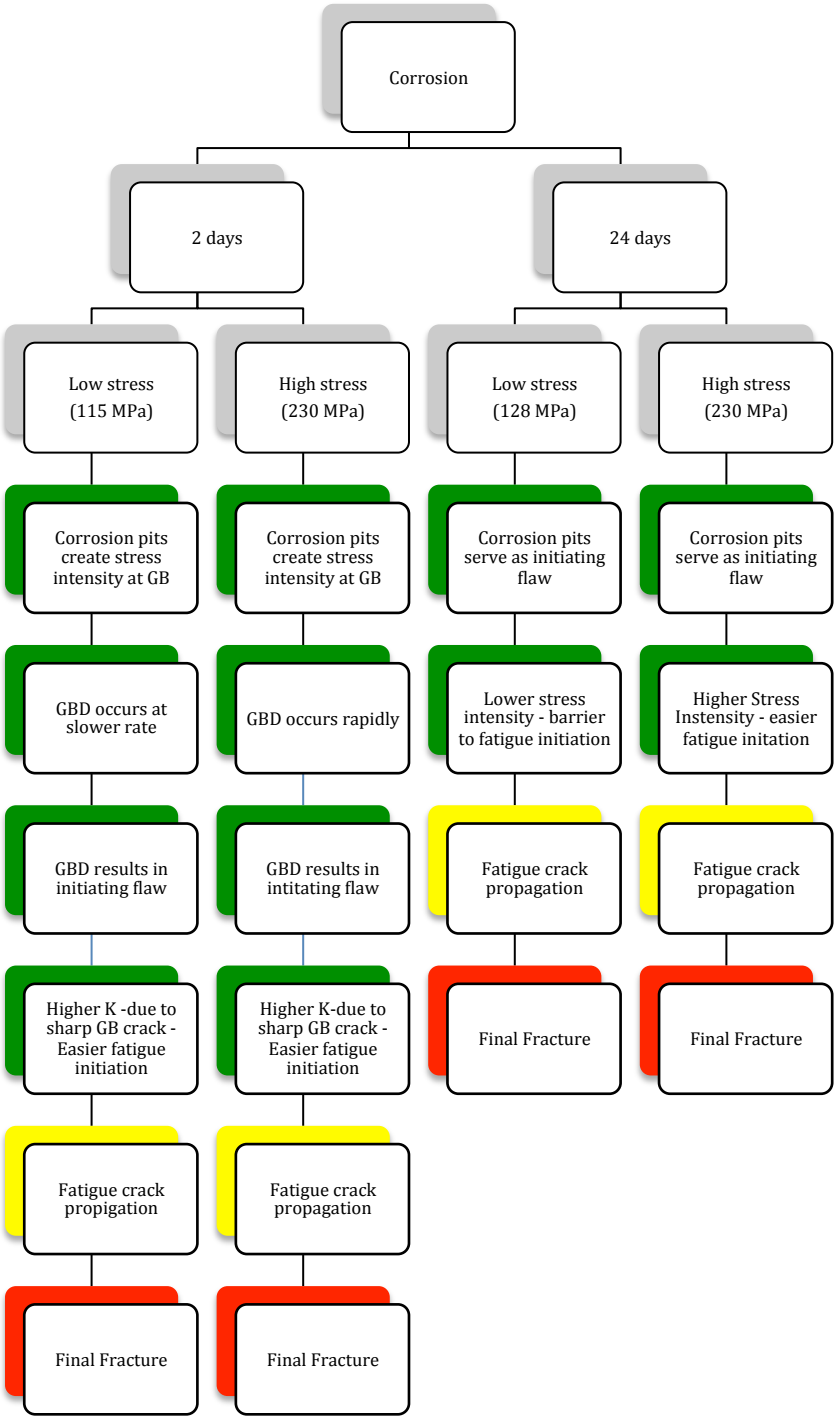

Figure 51: Summary flow chart of fatigue in corroded AA 6061-T6 in 3.5% NaCl at pH 2. Steps associated with fatigue initiation are shown with a green background, propagation with a yellow background, final fracture with a red background.

REFERENCES

1. Koch, G.H., et al., *Cost of corrosion study unveiled*, in *NACE international*2002, NACE: Houston, Tx.
2. Dieter, G.E., *Mechanical metallurgy*. 1986, New York: McGrawn Hill.
3. *Aluminum: Design and Application*. Aluminum, ed. K.R. Van Horn. Vol. II. 1967, Metals Park, Ohio: ASM.
4. Archer, R.S., Jefferies, Zay, *Aluminum base alloy*, U.s.P. office, Editor 1923.
5. Sanders, R.E., *Technology innovation in aluminum products*. JOM, 2001. **53**(2): p. 21-25.
6. Metals, A.S.f., *Aluminum. V.1. Properties, Physical Metallurgy and Phase Diagrams*. 1967: American Society for Metals.
7. Metals, A.S.f., *Properties and Selection: Nonferrous Alloys and Special-Purpose Materials*. Metals Handbook. 1990: American Society for Metals.
8. Hatch, J.E., A. Association, and A.S. Metals, *Aluminum: Properties and Physical Metallurgy*. 1984: A S M International.
9. Chakrabarti, D.J., Laughlin, D.E., *Phase relations and precipitation in Al-Mg-Si alloys with Cu additions*. Progress in Materials Science, 2004. **49**: p. 389-410.
10. Brandon, D. and W. Kaplan, *Microstructural Characterization of Materials*. 2 ed. 2008, West Sussex, England: John Wiley & Sons Ltd.
11. Edwards, G.A., Stiller, K., Dunlop, G.L., Couper, M.J., *The precipitation sequence in Al-Mg-Si alloys*. Acta Materialia, 1998. **46**(11): p. 3893-3904.
12. Marioara, C.D., Andersen, S.J., Jansen, J., Zandbergen, H.W., *The influence of temperature and storage time at RT on nucleation of the β phase in a 6082 Al–Mg–Si alloy*. Acta Materialia, 2003. **51**: p. 789-796.
13. Buha, J., Lumley, R.N., Crosky, A.G., Hono, K., *Secondary precipitation in an Al–Mg–Si–Cu alloy*. Acta Materialia, 2007. **55**: p. 3015–3024.
14. *Why Metal Fatigue Matters*, in *Metal Fatigue*. 2007, Springer Netherlands. p. 161-165.
15. Basquin, O.H., *The Exponential Law of Endurance Tests*. Proc. ASTM, 1910. **10**: p. 625-630.
16. Kun, F., et al., *Universality Behind Basquin's Law of Fatigue*. Physical Review Letters, 2008. **100**(9).
17. Collins, J.A., *Failure of Materials in Mechanical Design*. 2nd ed. 1993, New York: Wiley.
18. Tiryakioglu, M., P.D. Eason, and J. Campbell, *Fatigue life of ablation-cast 6061-T6 components*. Materials Science and Engineering A, 2012(559): p. 447-452.
19. Anderson, T.L., *Fracture Mechanics: Fundamentals and application*. 2005, Boca Raton, Fl: CRC Press.
20. Liu, H.T., et al. *Applications of abrasive-waterjets for machining fatigue-critical aerospace aluminum parts*. in *2009 ASME Pressure Vessels and Piping Conference, PVP 2009, July 26, 2009 - July 30, 2009*. 2010. Prague, Czech republic: American Society of Mechanical Engineers.

21. Forman, R.G. and S.R. Mattu, *Behavior of Surface and Corner Cracks Subjected to Tensile and Bending Loads in Ti-6Al-4V Alloy*, in *ASTM STP 1131*1992, American Society for Testing and Materials: Philadelphia, PA. p. 519-546.
22. Griffith, A.A., *The Phenomena of Rupture and Flow in Solids*. Philosophical Transactions, Series A, 1920. **221**: p. 163-198.
23. Wen, W. and T. Zhai, *Quantification of Resistance of Grain Boundaries to Short-Fatigue Crack Growth in Three Dimensions in High-Strength Al Alloys*. Metallurgical and Materials Transactions A, 2012. **43**(8): p. 2743-2752.
24. Takahashi, Y., et al., *Study on dominant mechanism of high-cycle fatigue life in 6061-T6 aluminum alloy through microanalyses of microstructurally small cracks*. Acta Materialia, 2012. **60**(6–7): p. 2554-2567.
25. Peralta, P., et al., *Effects of Local Grain Orientation on Fatigue Crack Growth in Multicrystalline fcc Metallic Materials*. Journal of Engineering Materials and Technology, 2005. **127**: p. 23-32.
26. Weertman, J., *Dislocation crack tip shielding and the Paris exponent*. Materials Science and Engineering: A, 2007. **468–470**(0): p. 59-63.
27. Weertman, J., *Rate of Growth of Fatigue Cracks Calculated from the Theory of Infinitesimal Dislocations Distributed on a Plane*. International Journal of Fracture Mechanics, 1966. **2**: p. 460-467.
28. Lawson, L., E.Y. Chen, and M. Meshii, *Near-threshold fatigue: a review*. International Journal of Fatigue, 1999. **21, Supplement 1**(0): p. S15-S34.
29. Irwin, G.R., *Fracture Dynamics*. Fracturing of Metals. 1948, Cleveland, OH: American Society for Metals.
30. Orowan, E., *Fracture and Strength of Solids*. Reports on Progress in Physics, 1948. **12**: p. 185.
31. Paris, P.C., M.P. Gomez, and W.P. Anderson, *A Rational Analytic Theory of Fatigue*. The Trend in Engineering, 1961. **13**: p. 9-14.
32. Paris, P.C. and F. Erdogan, *A Critical Analysis of Crack Propagation Laws*. Journal of Basic Engineering, 1960. **85**: p. 528-534.
33. Klesnil, M. and P. Lukas, *Influence of Strength and Stress History on Growth and Stabilisation of Fatigue Cracks*. Engineering Fracture Mechanics, 1972. **4**: p. 77-92.
34. McEvily, A.J., *On closure in Fatigue Crack Growth*, in *ASTM STP 982*1988, American Society for Testing and Materials: Philadelphia, PA.
35. Donahue, R.J., et al., *Crack Opening Displacement and the Rate of Fatigue Crack Growth*. International Journal of Fracture Mechanics, 1972. **8**: p. 209-219.
36. Walker, K., *The Effect of Stress Ratio During Crack Propagation and Fatigue for 2024-T3 and 7075-T6 Aluminum*, in *ASTM STP 1131*1970, American Society for Testing and Materials: Philadelphia, PA. p. 37-45.
37. Foreman, R.G., V.E. Keary, and R.M. Engle, *Numberical Anaysis of Crack Propagation in Cyclic-Loaded Structures*. Journal of Basic Engineering, 1967. **89**: p. 459-464.
38. Golden, P.J., A.F. Grandt Jr, and G.H. Bray, *A comparison of fatigue crack formation at holes in 2024-T3 and 2524-T3 aluminum alloy specimens*. International Journal of Fatigue, 1999. **21, Supplement 1**(0): p. S211-S219.

39. Lankford, J. and D.L. Davidson, *Fatigue Crack Micromechanisms in Ingot and Powder Metallurgy 7xxx Aluminum Alloys in Air and Vacuum*. Acta Metallurigca 1983. **31**: p. 1273-1284.
40. Laird, C., *Mechanisms and Theories of Fatigue*. Fatigue and Microstructure. 1979, Metals Park, OH: American Society for Metals.
41. Weibull, W., *Fatigue Testing and the Analysis of Results*. 1961, New York, Ny: Pergamon Press.
42. Weibull, W., *A Statistical Distribition Function of Wide Applicability* Journal of Applied Mechanics, 1951. **18**(3): p. 293-97.
43. Weibull, W. *A Statistical Theory of the Strength of Materials*. 1939.
44. Pierce, F.T., Journal of the Textile Institute, 1926. **17**: p. T355-T368.
45. Tiryakioglu, M. and J. Campbell, *Weibull Analysis of Mechanical Data for Castings: A Guide to the Interpretation of Probability Plots*. Metallurgical & Materials Transactions A, 2010. **41A**: p. 3121-3129.
46. Tiryakioğlu, M. and D. Hudak, *Guidelines for Two-Parameter Weibull Analysis for Flaw-Containing Materials*. Metallurgical & Materials Transactions. Part B, 2011. **42**(6): p. 1130-1135.
47. Tiryakioglu, M., *Relationship between Defect Size and Fatigue Life Distributions in Al-7 Pct Si-Mg Alloy Castings*. Metallurgical & Materials Transactions A, 2009. **40A**: p. 1623-1630.
48. Jones, D., *Principles and Prevention of Corrosion*. 1996, Upper Saddle River, NJ: Prentice-Hall.
49. Smialowska-Szklarska, Z., *Pitting corrosion of aluminum*. Corrosion Science, 1999. **41**: p. 1743-1767.
50. Zaid, B., Saidi, D., Benzaid, A., Hadji, S., *Effects of pH and chloride concentration on pitting corrosion of AA6061 aluminum alloy*. Corrosion Science, 2008. **50**: p. 1841-1847.
51. Boag, A., et al., *Stable pit formation on AA2024-T3 in a NaCl environment*. Corrosion Science, 2010. **52**(1): p. 90-103.
52. McCafferty, E., *Sequence of Steps in the Pitting of Aluminum by Chloride Ions*. Corrosion Science, 2003. **45**: p. 1421-1438.
53. Frankel, G.S., *Pitting corrosion of metals*. Journal of electrochemcial society, 1998. **145**(6): p. 2186-2198.
54. Janik-Czachor, M., G.C. Wood, and G.E. Thompson, British Corrosion Journal, 1980. **154**.
55. Gupta, R.K., et al., *Electrochemical Behavior and Localized Corrosion Associated with Mg2Si Particles in Al and Mg Alloys*. Electrochemistry letters, 2012. **1**(1): p. C1-C3.
56. Mutombo, K., *Intermetallic particles-induced pitting corrosion in 6061-t651 aluminum alloy*. Materials science forum, 2011. **690**(1): p. 389-392.
57. Harlow, D.G., *Constituent particle clustering and pitting corrosion*. Metallurgical & Materials Transactions A, 2011. **43**: p. 2832-2838.
58. Rajasankar, J. and N.R. Iyer, *A probability-based model for growth of corrosion pits in aluminium alloys*. Engineering Fracture Mechanics, 2006. **73**(5): p. 553-570.

59. Harlow, D.G., Wang, M.Z., Wei, R.P., *Statistical Analysis of Constituent Particles in 7075-T6 Aluminum Alloy*. Metallurgical & Materials Transactions A, 2006. **37A**: p. 3367-3373.
60. Birbilis, N., Cavanaugh, M.K., Buchheit, R.G., *Electrochemical behavior and localized corrosion associated with Al7Cu2Fe particles in aluminum alloy 7075-T651*. Corrosion Science, 2006. **48**: p. 4202-4215.
61. Schneider, O., et al., *In situ confocal laser scanning microscopy of AA 2024-t3 corrosion metrology - part 2 - trench formation around particles*. Journal of electrochemcial society, 2004. **151**(8): p. B464-B472.
62. Ilevbare, G.O., et al., *In situ confocal laser scanning microscopy of AA 2024-t3 corrosion metrology - part 1 - localized corrosion of particles*. Journal of electrochemcial society, 2004. **151**(8): p. B453-B464.
63. Ahn, J.J. and S. Ochiai, *Mechanical Behavior in the Silicon Carbide Reinforced Aluminum 6061 Composites Degraded by Room or High Temperature 3.5% NaCl Solution*. Journal of Engineering Materials and Technology, 2004. **126**(4): p. 436-442.
64. Wei, R.P., *A model for particle-induced pit growth in aluminum alloys*. Scripta Materialia, 2001. **44**(11): p. 2647-2652.
65. Liao, C.-M. and R.P. Wei, *Galvanic coupling of model alloys to aluminum — a foundation for understanding particle-induced pitting in aluminum alloys*. Electrochimica Acta, 1999. **45**(6): p. 881-888.
66. Wei, R.P., C.-M. Liao, and M. Gao, *A transmission electron microscopy study of constituent-particle-induced corrosion in 7075-T6 and 2024-T3 aluminum alloys*. Metallurgical & Materials Transactions. Part A, 1998. **29A**(4): p. 1153-1160.
67. Harlow, D.G. and R.P. Wei, *A probability model for the growth of corrosion pits in aluminum alloys induced by constituent particles*. Engineering Fracture Mechanics, 1998. **59**(3): p. 305-325.
68. Cawley, N.R., *Spatial statistics of particles and corrosion pits in 2024-t3 aluminum alloy*. Journal of Material Science, 1996. **31**(19): p. 5127-5134.
69. Dunwoody, B.J., Moore, D.M., Thomas, A.T., *The effect of incoherent particles on tougness of an Al-Mg-Si alloy*. Journal of the institute of metals, 1973. **101**: p. 172.
70. El-Menshawy, K., et al., *Effect of aging time at low aging temperatures on the corrosion of aluminum alloy 6061*. Corrosion Science, 2012. **54**(0): p. 167-173.
71. Baumgartner, M. and H. Kaesche, *Aluminum pitting in chloride solutions: morphology and pit growth kinetics*. Corrosion Science, 1990. **31**: p. 231-236.
72. Liang, W.J., et al., *General aspects related to the corrosion of 6xxx series aluminium alloys: Exploring the influence of Mg/Si ratio and Cu*. Corrosion Science, 2013. **76**: p. 119-128.
73. Dominguez Almaraz, G., V. Mercado Lemus, and J. Villalon Lopez, *Effect of Proximity and Dimension of Two Artificial Pitting Holes on the Fatigue Endurance of Aluminum Alloy AISI 6061-T6 Under Rotating Bending Fatigue Tests*. Metallurgical & Materials Transactions. Part A, 2012. **43**(8): p. 2771-2776.
74. Sankaran, K.K., Perez, R., Jata, K.V., *Effects of pitting corrosion on the fatigue behavior of aluminum alloy 7075-t6: modeling and experimental studies*. Materials Science and Engineering A, 2001. **297**: p. 223-229.

75. Priyantha, N., et al., *Localized Corrosion of Alloy 22 in Sodium Chloride Solutions at Elevated Temperature*. Corrosion, 2005. **61**(9): p. 857-871.
76. Harlow, D.G. and R.P. Wei, *Probability approach for prediction of corrosion and corrosion fatigue life*. AIAA, 1994. **32**(10): p. 2073 - 2079.
77. Cavanaugh, M.K., Buchheit, R.G., Birbilis, N., *Modeling the environmental dependance of pit growth using neural network approaches*. Corrosion Science, 2010. **52**: p. 3070-3077.
78. Liao, C.-M., G.S. Chen, and R.P. Wei, *A technique for studying the 3-dimensional shape of corrosion pits*. Scripta Materialia, 1996. **35**(11): p. 1341-1346.
79. Koul, M.G., *Topographical analysis of pitting corrosion in AA7075-t6 using laser profilometry*. Corrosion, 2003. **59**(7): p. 563-574.
80. Dolley, E.J., Lee, B., Wei, R.P, *The effect of pitting corrosion of fatigue life*. Fatigue & Fracture of Engineering Materials & Structures, 2000. **23**: p. 555-560.
81. Materials, A.S.f.T.a., *Variations in cross sectional shape of pits*, in *Standard Practive G 46-76*1988, ASTM: Philadelphia. p. 197.
82. Anderson, T.W. and D.A. Darlin, *A Test of Goodness-of-Fit*. Journal of the American Statistical Association, 1954. **49**: p. 765-769.
83. Yucel, E., *Modified Goodness-of-Fit Tests for the Weibull Distribution*, in *School of Engineering*1993, Airforce Institute of Technology.